

CHAPTER 4

vorgelegt von
Diplom-Physiker
Anton Haase
geboren in Berlin

Von der Fakultät II - Mathematik und Naturwissenschaften
der Technischen Universität Berlin
zur Erlangung des akademischen Grades
Doktor der Naturwissenschaften
Dr. rer. nat.

genehmigte Dissertation

Promotionsausschuss:

Vorsitzender: Prof. Dr. Mister Unbekannt
Gutachter: Prof. Dr. Stefan Eisebitt
Gutachter: Prof. Dr. Mathias Richter
Gutachterin: Dr. Saša Bajt

Tag der wissenschaftlichen Aussprache:

Berlin 2017

Berlin 2017

Tag der Wissenschaftlichen Aussprache:

Gutachterin: Dr. Sasa Bajt

Gutachter: Prof. Dr. Matthias Richter

Gutachter: Prof. Dr. Stefan Eisebitt

Vorsitzender: Prof. Dr. Misster Unbekannt

Promotionsausschuss:

genehmigte Dissertation

Dr. rer. nat.

Doktor der Naturwissenschaften

zur Erlangung des akademischen Grades

der Technischen Universität Berlin

Von der Fakultät II - Mathematik und Naturwissenschaften

geboren in Berlin

Anton Haase

Diplom-Physiker

vorgelegt von

CHAPTER 4

Contents

1	Introduction	1
2	Theoretical Description of EUV and X-ray Scattering	5
2.1	EUV and X-ray Radiation	5
2.2	Interaction of EUV and X-ray Radiation With Matter	6
2.2.1	Elastic Scattering	9
2.2.2	Absorption and Fluorescence	11
2.3	Specular Reflection from Surfaces and Interfaces in Layered Systems	12
2.4	Diffuse Scattering in Layered Systems	15
2.5	Grazing-incidence X-ray Fluorescence	22
3.1	Synchrotron Radiation	27
3.2	The Instrumentation for the EUV Spectral Range	31
3.2.1	The EUV Beamlines at BESSYII and MLS	31
3.2.2	The Experimental Endstations at the EUVR and SX700 Beam-lines	33
3.3	Grazing-incidence X-ray Fluorescence at the FCM Beamline	36
3.4	Sample systems	37
3.4.1	Choice of the Chemical Species and Multilayer Design	38
3.4.2	Multilayer Deposition by Magnetron Sputtering	39
4	Characterization of the Multilayer Structure for Different Systems	41
4.1	Reconstruction Based on Specular EUV reflection	42
4.1.1	Multilayer Model and Particle Swarm Optimization	44
4.1.2	Model Uniqueness and Maximum Likelihood Estimation	47
4.2	Molybdenum Thickness Variation in Mo/Si/C Multilayers	51
4.2.1	Sample systems and experimental procedure	52
4.2.2	Combined Analysis of X-ray and EUV reflectance	54
4.2.3	Optimization results	59
4.3	Analysis of Cr/Sc Multilayers with Sub-nanometer Layer Thickness	62
4.3.1	Reconstruction with a discrete layer model approach	63

4.3.2	Extending The Model to Graded Interfaces and Interdiffusion	99
4.3.3	Addition of Complementary Experimental Methods	72
4.3.4	Reconstruction and Maximum Likelihood Evaluation	74
5 Analysis of Interface Roughness based on Diffuse Scattering		83
5.1	Near-normal Incidence Diffuse Scattering	83
5.1.1	Mapping Reciprocal Space and Bragg Sheets	84
5.1.2	Kreszig-like Peaks and Resonant Effects	86
5.1.3	Reconstruction of the PSD and the Multilayer Enhancement Factor	88
5.2	Roughness for Varying Mo Thickness in Mo/Si Multilayer Samples	91
5.2.1	Tilted Bragg Sheets	92
5.2.2	Reconstruction of the Power Spectral Density	93
5.3	Solving the Roughness Correlation in Cr/Sc Multilayer Samples	95
6 Summary and Outlook		99
References		101

In this chapter we analyze the structural properties of different multilayer systems. The samples investigated here are highly periodic multilayer systems designed as mirrors to reflect radiation in different spectral ranges. The basic theory behind ^{Al}_x^{Ti}_{1-x} of a one-dimensional Bragg crystal exploited to achieve high reflectance values, is described in chapter 2. All systems were fabricated using the magnetron sputtering technique in chapter 2. All systems were fabricated using the magnetron sputtering technique two different wavelength ranges within the extreme ultraviolet (EUV) spectrum, the range from 12.4 nm to 14.0 nm and the so-called water window range from 2.2 nm to 4.4 nm. As discussed in Sec. 2.3 of Ch. 2, the individual layer thicknesses and the required number of periods are intrinsically connected to the spectral range and angles, where maximum reflectance shall be achieved. In case of the systems analyzed within this chapter, the individual layer thicknesses are ranging from approximately 4 nm down to 0.5 nm. In addition, each periodic part of the multilayer system is composed out of two to four of these individual layers ~~that repeated with a number of periods of 50 to 400~~. For the performance of a multilayer mirrors system, the surface and interface morphology and the actual layer thicknesses and densities of all these layers play a crucial role and affect the reflectivity behavior. Small deviations of the perfect layer layout such as intermixing or roughness at the interfaces are therefore a significant reason for a diminished reflectivity. While the deposition through the magnetron sputtering process is a well established technique for mirror fabrication, the actual layer thicknesses in the sample may differ from the nominal values and furthermore have imperfections at the interfaces. For an improvement of the deposition process, it is thus essential to assess the sample morphology and potential intermixing of these highly complex samples.

Characterization of the Multilayer Structure for Different Systems



The sample was measured with respect to its reflectivity across the spectral range mentioned above at an angle of incidence of $\alpha_i = 15^\circ$ from the surface normal. The

in Fig. 4.2.

S. O. 2?

of the layer layout can be found in the description of the corresponding theoretical figure but terminates at the vacuum interface with the silicon layer. A detailed schematic figure system is $N = 65$, while the 65th (capping) layer period does not possess a carbon layer within one period from bottom to top as Mo/B₄C/Si/C. The number of periods for that interfaces, respectively. We shall therefore refer to this sample with the layer sequence layers of boroncarbide (B₄C) and carbon (C) were included at the Mo to Si and Si to Mo problem of intermixing and resulting loss of interface definition, additional barrier sample contains a periodic layer stack of molybdenum (Mo) and silicon (Si). Due to coating was deposited with magnetron sputtering on a polished silicon substrate. The multilayer semiconductor industry, for which this sample served as a prototype. The multilayer combination is of relevance for optical setups in the next generation lithography for peak in the reflectance at a wavelength of $\lambda = 13.5$ nm for an angle of incidence of $\alpha_i = 6^\circ$. solely on experimental data of EUV reflectivity. The mirror was designed to achieve a normal incidence mirror for the wavelength range between 12.4 nm and 14.0 nm based In this section we demonstrate the reconstruction of a multilayer system designed as near-

4.1 Reconstruction Based on Specular EUV reflectance

This chapter is structured as follows. First, the information content within a simple reflectivity curve for the design wavelength of the mirrors systems is discussed in Sec. 4.1 at the example of a mirror for the EUV range between 12.5 nm and 14.0 nm. A reconstruction of the model for that particular system is presented and discussed in Sec. 4.2, the investigation of a more complex set of samples designed for the same spectral range is conducted. Here, the individual layer thicknesses inside the samples were varied and different polishing methods affecting the interface morphology were applied during fabrication. Based on the analytical experiments conducted here, an improved reconstruction could be obtained by incorporating data from additional X-ray reflectivity (XRR) experiments. Finally, in Sec. 4.3, multilayer mirrors with sub-nanometer thicknesses for the water window spectral range are investigated as limiting case of very thin layer systems. There, the combination of multiple analytical experiments is required to deduct a consistent reconstruction of the model.

In Sec. 4.1, the goals during the fabrication process, into a model of that system. Starting from design goals by accumulating prior knowledge about the sample, such as the nominal reverse problem by reverse engineering the layer properties is therefore an attempt of solving this scatterometry. Reconstruction of the inverse problem of that particular system is presented and discussed in Sec. 4.2, the methods to assess the uniqueness and parameter accuracy. Second, conjunction with methods to reconstruct the thicknesses inside the samples in Sec. 4.2, the investigation of a more complex set of samples designed for the same spectral range is conducted. Here, the individual layer thicknesses inside the samples were varied and different polishing methods affecting the interface morphology were applied during fabrication. Based on the analytical experiments conducted here, an improved reconstruction could be obtained by incorporating data from additional X-ray reflectivity (XRR) experiments. Finally, in Sec. 4.3, multilayer mirrors with sub-nanometer thicknesses for the water window spectral range are investigated as limiting case of very thin layer systems. There, the combination of multiple analytical experiments is required to deduct a consistent reconstruction of the model.

The reconstruction of a given model based on the evaluation of EUV (or XRR) model for the reconstruction. Effectivity data is a well established method for the characterization of multilayer systems [7, 24, 68]. In most cases a model is optimized applying gradient methods such as the Levenberg–Marquardt method [66, 73]. Those optimization algorithms typically operate with a set of start parameters within the parameter space and iteratively improve an optimization function usually termed χ^2 , describing the sum of the squared absolute value of the difference between the theoretical calculation and the experimental data. This is done by calculating the gradient of a that function in all directions in the parameter space and changing the parameters accordingly in direction of smaller χ^2 values. This approach has the major disadvantage that the end result is strongly dependent on the choice of starting values and may not represent a global minimum of χ^2 but only a local optimum. While estimations of the quality of the fit results within the (local) optimum are possible, no estimation can be given globally for the given model. For those reasons, this characterization strategy has only limited applicability and alternative approaches are possible.

The reflectivity curve shows a broad peak attaining its maximum value at a wavelength of approximately 13.1 nm, which is lower than the design peak reflectance of 13.5 nm. That is due to the different angle of incidence used in the experiment. Apart from the main peak, side fringes are visible. They originate from the superposition of waves being reflected at the top surface and the substrate interface. They are thus directly related to the total thickness of the multilayer coating and well known as *Kissig fringes* [60]. Based on the data obtained through this spectral resolved reflectivity experiment, we shall attempt to reconstruct the unknown layout in the following sections. The nominal fabrication parameters serve as starting values for the analysis to build a reasonable

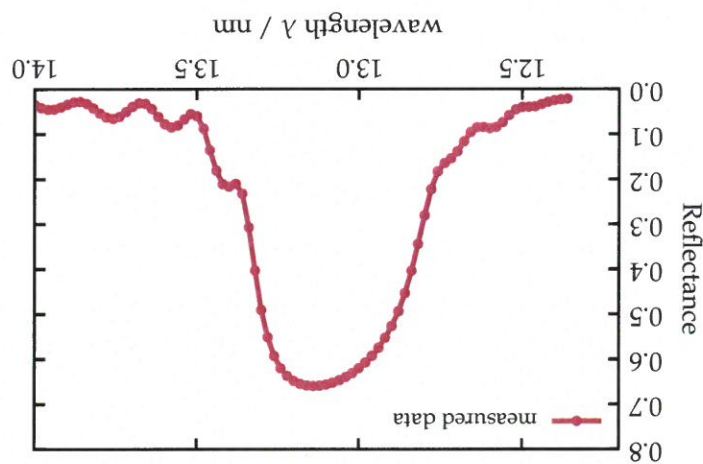
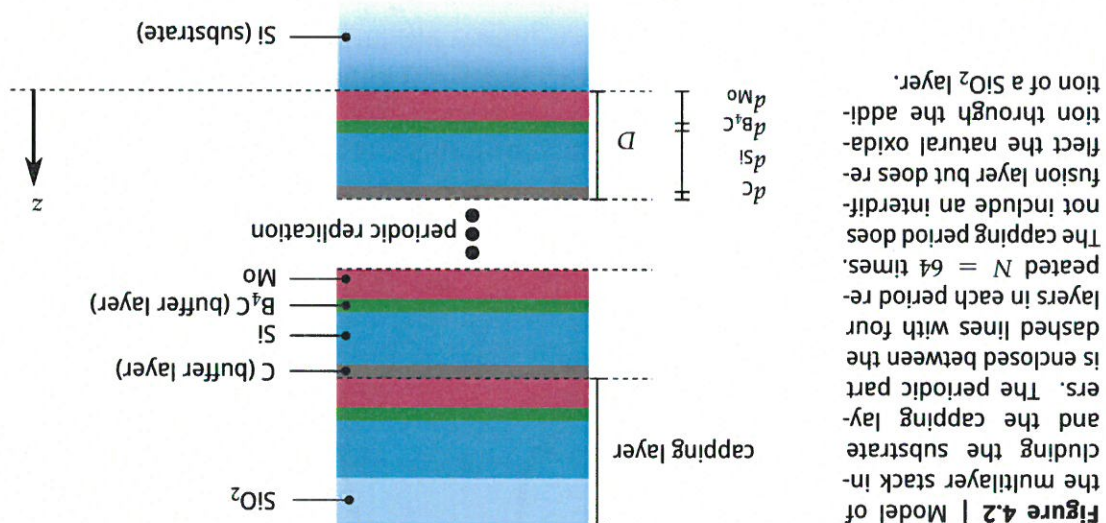


Figure 4.1 Spectrally resolved reflectance of the Mo/B₄C/SiC multi-layer sample. The measured spectrum was conducted under a fixed angle of incidence $\alpha_i = 15.0^\circ$.

measurement was conducted at the extreme ultraviolet beamline (EUVR) beamline at the metrology light source (MLS). The reflectivity was evaluated by first measuring the intensity of the direct beam in the reflectometer with the photo diode detector. Then, the reflected radiation at an angle of 30° was measured in reference to the direct beam signal. To ensure the stability of the result, the direct beam was measured again afterwards and compared to the data of the first measurement. The normalized results are shown in Fig. 4.1. The measurement uncertainty with this experimental method is within 0.15% (one standard deviation) of the peak reflectance value [91] and an angular uncertainty of 0.10°, which leads to an upper limit for the total uncertainty margin is within curve of 0.4% in the peak flanks. Consequently, the total uncertainty margin is within the line thickness of the data presentation in Fig. 4.1.

shows the first order Bragg peak of the layer system, none of the layers can be thicker each of the parameters. Due to the fact that the EUV reflectivity curve shown in Fig. 4.1 multilayer sample can be found in table 4.1 together with physically plausible limits for each calculation based on the matrix algorithm. A full list of the model parameters for the are taken from values by Henke et al. [53] and are used for the theoretical range i.e. the indices of refraction, of the respective materials in the relevant spectral range interferences as introduced in chapter 2 is also included. The required optical constants, finally, the Nevo-Croce factor α accounting for roughness and interdiffusion at the silicon dioxide layer. Each of the deposited layers may vary in density with respect to the bulk density of that material [24], which also needs to be reflected in the model. is given by the thicknesses of each layer within one period as well as for the capping be taken into account through a silicon dioxide layer. The parameterization of that model ambient conditions, a passivation of the top silicon surface through oxidation has to mississing carbon interdiffusion layer on the top surface. Since the sample was exposed to replicated 64 times. With the top period being different from the others through the introduced above, the multilayer coating consists of a periodic arrangement of four layers



For the purpose of reconstructing the layout of the Mo/B₄C/Si/C sample, a parameterized model is needed entailing the theoretical calculations to obtain the reflectivity curve according to the matrix algorithm. The model is largely based on prior knowledge available from the fabrication process. For the multilayer sample investigated here, the nominal layer design is known and a schematic representation is shown in Fig. 4.2. As curve of the multilayer stack in- cluding the substrate and the cappling layer and the cappling layer is enclosed between the dashed lines with four layers in each period four repeated $N = 64$ times. The capping period does not include an interdif- fusion layer but does re- fuse the natural oxide ad- dition through the addi- tion of a SiO₂ layer.

In contrast to those gradient methods, heuristic optimization algorithms exist. Instead of operating with predefined starting values, from which a gradient approach minimizes the χ^2 functional, they operate distributed on the whole parameter space with often randomly initialized parameters within given boundaries, instead. In the following we shall apply those heuristic optimization routines to obtain the reconstruction of the Mo/B₄C/Si/C sample and elaborate their application to the characterization of multilayer systems in detail.

algorithm known as particle swarm optimization (PSO) [59]. In contrast to the afore-
For the minimization of the functional in Eq. (4.1) we apply a global optimization

measurment point is described by \vec{q}_m .

wavelength associated with measurment point m . The experimental uncertainty for each R in Eq. (2.28) in chapter 2. Each point is calculated based on the angle of incidence and reflectivity curve above I_m^{model} follows directly from the matrix algorithm and the quantity EUV with index m having the measured intensity I_m^{meas} . The calculated intensity for the EUV the model, I_m^{model} is the calculated intensity for the corresponding measuring point where M is the number of measurement points, P is the number of parameters used in

$$\chi^2 = \frac{1}{M-P} \left[\sum_{m=1}^M \frac{(I_m^{\text{model}} - I_m^{\text{meas}})^2}{(I_m^{\text{meas}})^2} \right], \quad (4.1)$$

on the method of least squares [14, 43, 65] and the functional is defined as the reduced χ^2 goodness of the model with respect to the measured data. The quality is asserted based problem. Based on the measured reflectivity data an optimization functional defines the As introduced above, the reconstruction of the multilayer is an optimization

principally

The minimization functional and particle swarm optimization

the generality.
the measured peak reflectance can not be attained within this model thus not limiting value of the Nevo-Croce factor was limited to be below $a \leq 2 \text{ nm}$. With its upper limit, the theoretical limit of the multilayer sample in the EUV measurement, the maximum the bulk density, on the other hand, is unlikely. Due to the high peak reflectance close to crystalline structure, the bulk density may not be attained. A layer with a density above of the deposited layers. Through possible defects in an amorphous layer compared to a is introduced to take into account reduced layer densities due to the amorphous state was constrained to values between 50 % and 100 % with respect to their bulk density. This attain thicknesses below 1 nm. The density of the various materials within this model than 7 nm, i.e. in the order of half of the wavelength. The barrier layers were designed to

Parameter	Definition	Lower bound	Upper bound
$d_{\text{Mo}} / \text{nm}$	Mo layer thickness	0.0	7.0
$d_{\text{Si}} / \text{nm}$	Si layer thickness	0.0	7.0
d_{C} / nm	C buffer layer thickness	0.0	5.0
$d_{\text{B}^4\text{C}} / \text{nm}$	B^4C buffer layer thickness	0.0	5.0
a / nm	Nevo-Croce parameter	0.0	2.0
$d_{\text{Mo}} / \text{nm}$	Mo density wrt. bulk density	0.5	1.0
$d_{\text{Si}} / \text{nm}$	Si density wrt. bulk density	0.5	1.0
d_{C} / nm	C density wrt. bulk density	0.5	1.0
$d_{\text{B}^4\text{C}} / \text{nm}$	B^4C density wrt. bulk density	0.5	1.0
$d_{\text{SiO}_2(\text{cap})} / \text{nm}$	SiO ₂ capping layer thickness	0.0	5.0
$d_{\text{SiO}_2(\text{cap})}$	$= d_{\text{Si}}$ (identical to Si density)		

Table 4.1 | Multilayer parameterization and parameter limits

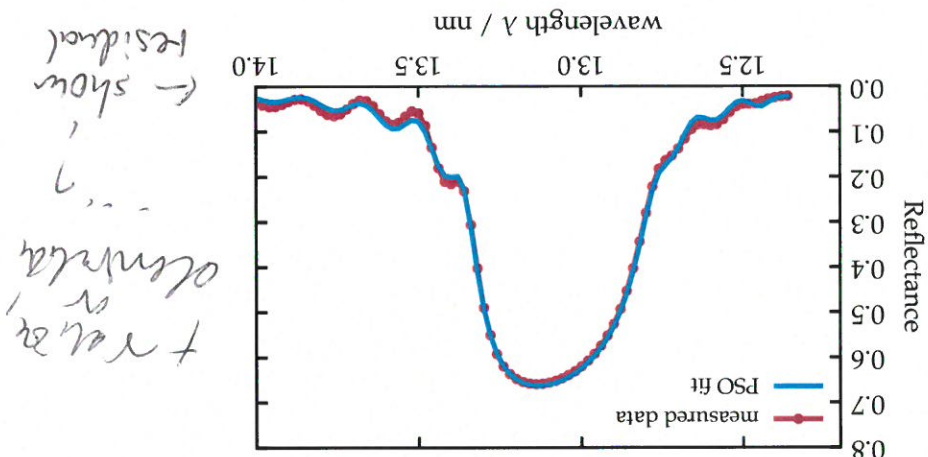


Figure 4.3 | Theoretical reflectance curve based on the optimal model parameters obtained from the particle swarm optimization.

We have applied this optimization procedure to the Mo/B₄C/Si/C sample and the measured EUV reflectivity curve. The fit result is shown together with the measured data in Fig. 4-3. The parameter results are listed in table 4-2. The solution does indeed provide

Model reconstruction based on the EUV reflectivity data

mentioned gradient based methods, the PSO operates on the whole parameter space as defined by the upper and lower parameter limits, which are given in table 4.1 for the particular example here, without specific starting parameters influencing the convergence. We implemented the PSO algorithm based on the draft by Carlisle and Dozier [25]. The basic mechanism of the algorithm is the definition of a swarm of individuals [25]. The basic mechanism of the PSO algorithm is the definition of a swarm of individuals, which are initialized randomly distributed across the allowed parameter space. Particles, each of those particles calculates the minimization function at its random position retaining that result including a random start velocity. In an iterative process, the position retains the result including a random start velocity. Within that iteration each of velocity vector within the parameter space for each particle. Within that iteration each of the particle thus moves to a new position, where the minimization function is again evaluated and compared the the individual and global best solutions. If a better value is found, the respective retained results are updated with the new value and the next iteration is performed. While following that process the particles eventually converge to the global best solution, which may or may not be the global best optimum of the whole optimization problem. Due to the combination of social and cognitive component, fast convergence into a local optimum can be avoided. The state of full convergence is reached, when either all particles occupy the same place in the parameter space or it stagnation is reached. Due to the heuristic nature of the algorithm, it may happen that the global best optimum found is not necessarily the global minimum of the optimization problem. The result may be verified, however, by repeated application of the algorithm or simply by reaching a satisfactory solution through comparison of the measured and calculated curves and thus small χ^2 values.

With the ambiguous reconstruction result of the previous section, the demand for a verification of uniqueness with respect to the measured data becomes apparent. To clarify the problem of uniqueness of the solution, it is instructive to investigate the influence of the individual model parameters on the theoretical reflectivity curve. In Fig. 4.4 we varied a subset of the parameters starting from the PSO solution from Sec. 4.1.1. In each of the subfigures, one parameter or a quotient of parameters is varied while all others are kept fixed. By comparison of Fig. 4.4a, 4.4b, 4.4c and 4.4e it becomes clear that a reduction of the peak reflectivity can originate in either a large roughness and interdiffusion parameter or similarity from the thickness of the capping layer, the silicon to molybdenum layer thickness ratio of the molybdenum density. A reconstruction based on a single EUV reflectivity therefore intrinsically produces a highly ambiguous result in this case, does not allow for a unique set of parameters of the model minimizing the χ^2 functional. In reality multiple solutions with very similar values for χ^2 exist as shown above. Clearly, this raises the question of how accurately a reconstruction may be achieved here.

4.1.2 Model Uniqueness and Maximum Likelihood Estimation

Parameter	Definition	PSO results	χ^2	reduced χ^2 value	17.87	17.89	18.27
$d_{SiO_2(cap)}$ / nm	SiO ₂ capping layer thickness	3.194 3.418 3.558	p_{B4C}	B ₄ C density w.r.t. bulk density	0.909	0.973	0.936
d_{Mo} / nm	Mo layer thickness	2.460 2.748 3.082	p_C	C density w.r.t. bulk density	0.833	0.971	0.608
d_{Si} / nm	Si layer thickness	2.421 2.617 1.997	p_{Si}	Si density w.r.t. bulk density	0.883	0.974	0.749
d_C / nm	C buffer layer thickness	0.811 0.709 0.818	p_{Mo}	Mo density w.r.t. bulk density	0.989	0.919	0.944
d_{B4C} / nm	B ₄ C buffer layer thickness	1.308 0.923 1.129	a / nm	Nevo-Croce parameter	0.322	0.249	0.177
d_{SiO_2} / nm	SiO ₂ capping layer thickness	3.194 3.418 3.558					

Table 4.2 | Results for the optimized parameters based on the PSO of the EUV reflectivity for the Mo/B₄C/Si/C sample.

the characterization additional methods of model verification are thus required. We shall therefore discuss an additional approach to the optimization problem in the following section on how the model validity and the information content of the measured data can be asserted based on the example of the PSO results obtained here.

Reconstruction Based on Spectral EUV reflectance

$$L(M(\bar{x})|E) \propto L(E|M(\bar{x}))L(M(\bar{x})), \quad (4.3)$$

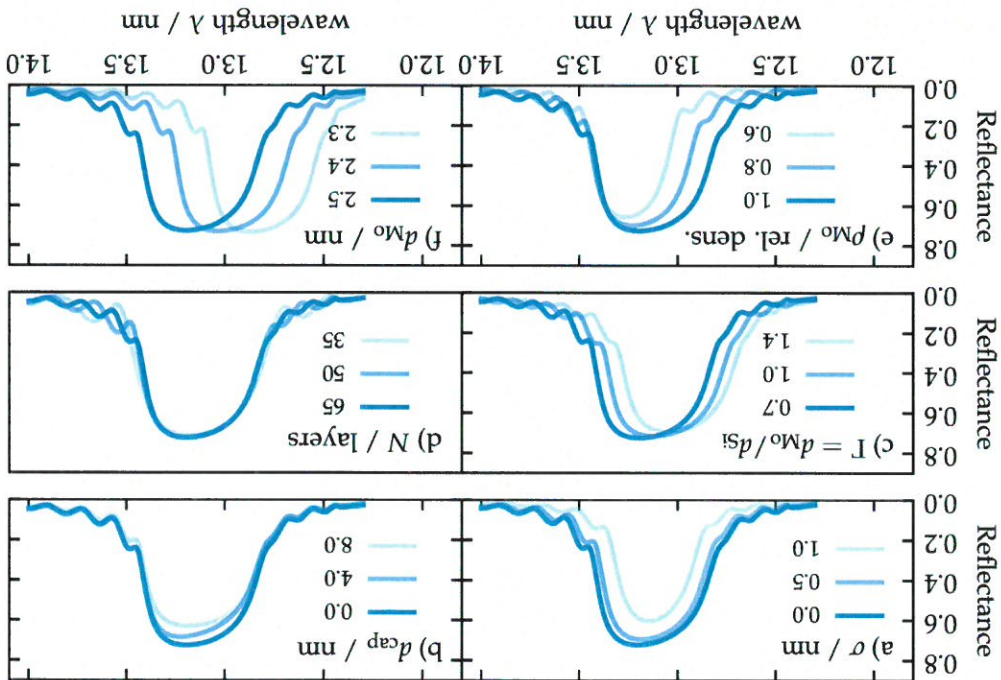
where E denotes the experiment, i.e. the measured data and $M(\bar{x})$ represents the model given through parameter set \bar{x} , e.g. the parameters of the model in table 4.1. In our case however, we seek to evaluate the likelihood $L(M(\bar{x})|E)$ that the model $M(\bar{x})$ with a given set of parameters \bar{x} is valid assuming the experiment E yields the correct curve (the so called "posterior distribution"). Those two quantities are linked through the Bayesian theorem [11, 76] stating

$$L(E|M(\bar{x})) \propto \exp(-\chi^2(\bar{x})/2), \quad (4.2)$$

under the assumption that the model is correct is proportional to form [1]. Thus, the likelihood that the measured values match with the theoretical curve assumed to be obtainable exactly through the theoretical calculation, is then of Gaussian function for a measurement result matching with the actual reflectivity curve, which is assumed Gaussian uncertainties for the experiment. The corresponding probability density distributed around the actual reflectivity curve following a Gaussian distribution, i.e. we assume independent measurements. We further assume that any measured point is assuming independent measurements. A solution of the aforementioned problem is evaluated based on a non-centered χ^2 distribution of model and experiment result is evaluated based on a non-centered χ^2 distribution of mirrors has been demonstrated by Hobson and Baldwin [55]. In our case, the match method [47]. An application of this technique to the design process of multilayer by numerically sampling the functional based on a Markov-chain Monte Carlo (MCMC) vicinity of the PSO solution or possibly the whole parameter space. We approach this solution of the aforementioned problem requires to determine the value of χ^2 in

Maximum likelihood

Figure 4.4 | Influence of the change of parameter model on the simulated EUV reflectivity curve. In each of the figures, all parameters were kept constant at the values listed in table 4.2 varying only the respective shown parameter.



CHARACTERIZATION OF THE MULTILAYER STRUCTURE FOR DIFFERENT SYSTEMS

We have applied an existing implementation of the MCML algorithm by Foreman-Mackey et al. [42] to the EUV measurement of the Mo/B₄C/Si/C sample in Fig. 4.1 with the model in Fig. 4.2. The likelihood, as defined in Eq. (4.4) with the χ^2 function from Eq. (4.1), is sampled in a high-dimensional space depending on the number of parameters in the model. We therefore need to project the distribution for each parameter by marginalizing over all other parameters. Alternatively, two-parameter correlations can be visualized by projecting on a two-dimensional area, again marginalizing across all other parameters. The projection for the Si and Mo layer thicknesses are shown in Fig. 4.5b and 4.5c. In both cases, a well defined distribution is obtained. In the two-dimensional projection in Fig. 4.5a, no correlations are apparent and a two-dimensional Gaussian-like shape results. In all cases, the one-sigma standard deviations for Gaussian distributions are shown together with the weighted center, i.e. the 50th percentile. The PSO result is also indicated, which is compatible with the one sigma standard deviation, but does not match the center of the likelihood result. The reason for that lies in higher order correlations of the parameters. In Fig. 4.6, all one-dimensional projections of the likelihood distribution are shown for all remaining parameters. Clearly, while a reasonably small confidence interval (again, one standard deviation for all distributions) can be found for the thickness of the carbon and boroncarbide layers, the off-center value for the silicon thickness of the PSO result in Fig. 4.5c is compensated by a larger than center value for the boroncarbide layer in Fig. 4.6. Thus, the thicknesses are correlated and are no independent model.

Confidence intervals for the Mo/B₄C/SiC sample

Solving the optimization problem posed in the previous section within this context, the MCMC method poses a statistical approach on evaluating (mapping) the likelihood function $L(x)$. It was proven that after a theoretical number of infinite iterations, the distribution of the individual samples within the MCMC algorithm, corresponds to the likelihood function in Eq. (4.4) [26, 71]. With a limited number of iterations, a numerical approximation of that distribution is obtained after reaching an equilibrium state in the algorithm [42]. It thus yields an alternative method on solving the optimization problem by extracting the maximum likelihood from the final result. However, in addition to the maximum value, confidence intervals for each of the parameters can be quantified within the one- or two-sigma standard deviations of the data. The likelihood distribution in parameter space is obtained allowing to extract confidence intervals for each of the parameters. Thereby, the aforementioned ambiguity of solutions can be quantified within the available experimental data.

$$L(\vec{x}) = L(M(\vec{x})|E) \propto \exp\left(-\chi^2(\vec{x})/2\right) L(M(\vec{x})). \quad (4.4)$$

where $L(M(\bar{x}))$ denotes the likelihood function for the model to be valid for a specific set of parameters \bar{x} (the so called "prior distribution"). The prior distribution does contain any prior knowledge about the model and allowed parameters. For the example of the model outside the listed boundaries and $L(M(\bar{x})) = 1$ everywhere else. In addition, we limit the maximum total period thickness, i.e. the sum of all layers in one period to only allow the appearance of the first Bragg peak within the measured spectral range through the same condition. Combining Eq. (4.2) and Eq. (4.3) then yields the likelihood function

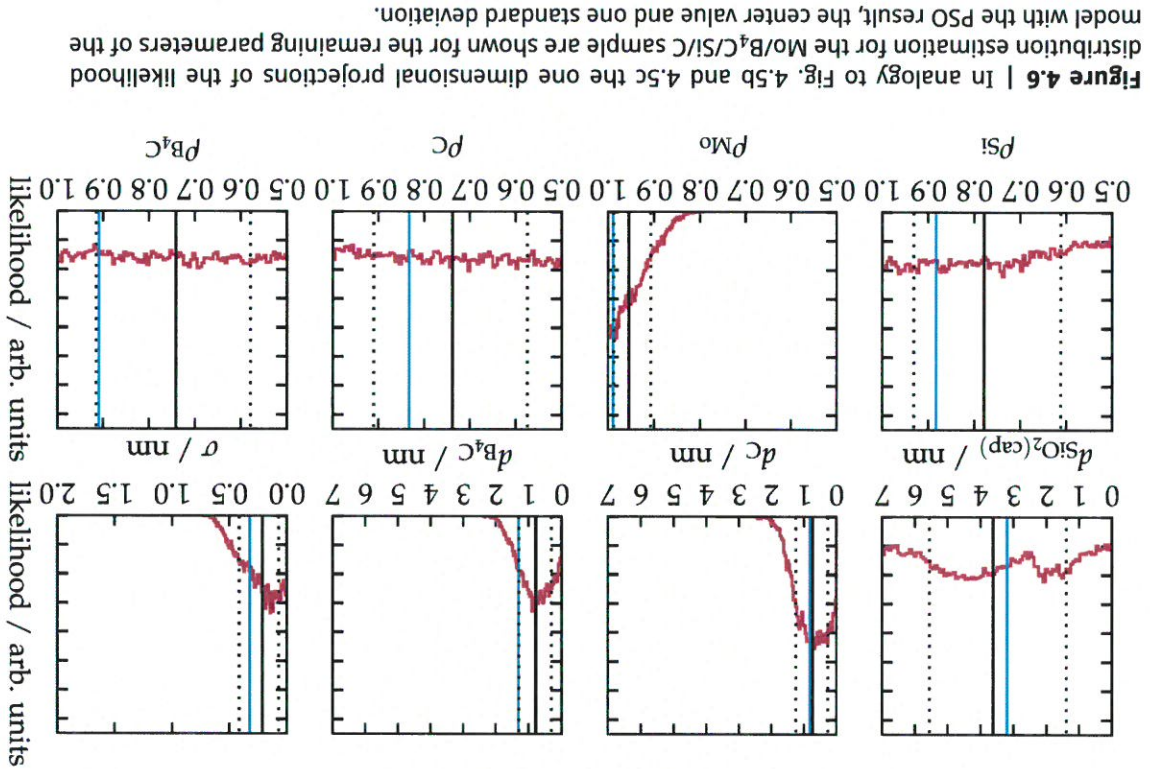
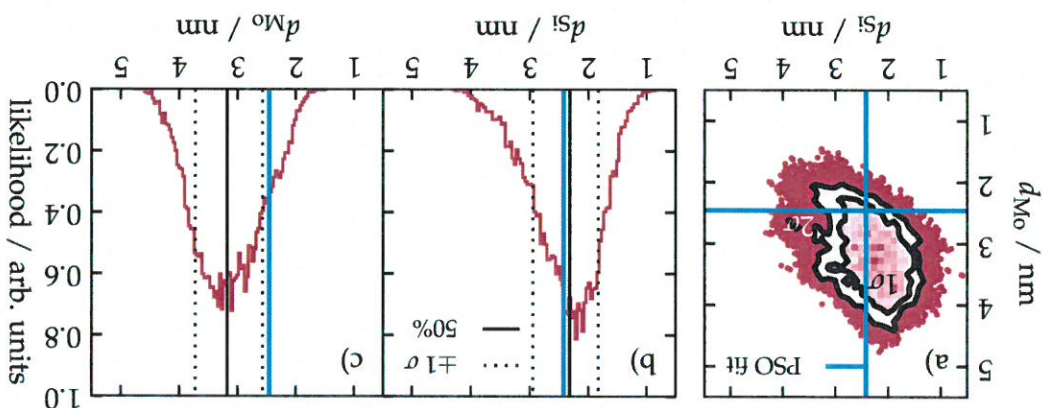


Figure 4.5 | Results of the maximum likelihood estimation obtained via the MCMC procedure. a) Two dimensional projection of the likelihood distribution for the parameter pair d_{Si} and d_{Mo} . The projection was obtained by marginalizing over all other parameters of the model. The projection was obtained by marginalizing over all other parameters of the model. b) One dimensional projections for one and two standard deviations (one and two sigma contours). The black contours indicate the areas found with the PSO method. c) The one dimensional distribution similarly to b) for the molybdenum layer thickness.



For the engineering of a near-normal incidence mirror, the ratio of molybdenum layer thickness to total period thickness has a clear impact on the reflectivity curve as seen from the theoretical simulations in Fig. 4-4c. Studies have shown, that an optimal value for the high reflectivity is achieved by depositing 40% molybdenum layer thickness d_M with respect to the total period thickness D [7, 24]. During the deposition process, the layer of molybdenum grows in thickness and at a certain threshold, crystallites may begin to

tilayers

4.2 Molybdenum Thickness Variation in Mo/Si/C Multi-layers

It should be noted, that the given center values here are not a good solution to the optimization problem. The reason for that is, that the parameters are highly correlated. The center values of the one-dimensional projections may therefore not be suitable parameters for the model based on the low amount of data available. A valid optimization result can therefore only be obtained by either applying the PSO routine or by iterative application of the MCMC procedure. The latter may be achieved by fixing single parameters according to their maximum likelihood value found in the previous iteration and obtaining the resulting likelihood distributions for the remaining parameters according to that restricted prior distribution.

Parameter	PSO result	center value	1σ c.i.	2σ c.i.
$d_{SiO_2(cap)}/\text{nm}$	3.194	3.677	(-2.252/+1.94)	(-3.407/+3.108)
d_{Mo}/nm	2.460	3.137	(-0.587/+0.560)	(-1.054/+1.016)
d_{Si}/nm	2.421	2.338	(-0.497/+0.616)	(-0.916/+1.294)
d_{C}/nm	0.811	0.744	(-0.477/+0.510)	(-0.696/+0.971)
d_{B4C}/nm	1.308	0.782	(-0.471/+0.511)	(-0.722/+0.973)
a/nm	0.322	0.214	(-0.143/+0.201)	(-0.204/+0.347)
q_{Mo}	0.989	0.953	(-0.048/+0.034)	(-0.094/+0.045)
q_{Si}	0.883	0.782	(-0.167/+0.147)	(-0.264/+0.208)
q_{C}	0.833	0.739	(-0.164/+0.175)	(-0.228/+0.249)
q_{B4C}	0.909	0.741	(-0.162/+0.172)	(-0.230/+0.247)

Table 4.3 | MCMC results obtained by the analysis of the EU reflectivity for the Mo/B₄C/SiC sample. The center values (50% percentile) together with confidence intervals (c.i.) of one and two standard deviations are shown.

parameters. Nevertheless, confidence intervals can be obtained within the given model and the given prior (the boundaries listed in table 4.1) and are listed accordingly in table 4.3 for one and two standard deviations. Within the allowed boundaries, some parameters remain entirely undefined with similar likelihood for any parameter value, such as the SiO₂ capping layer thickness, the silicon, carbon and boroncarbide relative densities. Their corresponding total confidence intervals thus cover almost exactly 68.2% (one standard deviation) and 95.4% (two standard deviations) of the allowed respective parameter range. Hence, with respect to the model defined and the measured EUV reflectivity curve, no reliable value for those sample properties can be determined.

Two sets of several samples of Mo/Si/C multilayer mirrors with C interdiffusion barriers with thicknesses of nominally below 0.5 nm at the Mo on Si interfaces (a detailed figure of the model for those samples is given below in Fig. 4.9 of the following sections) were prepared. As mentioned above, the samples under investigation here were fabricated with increasing relative Mo thickness from sample to sample while keeping the nominal period thickness $D \approx 7$ nm constant by correspondingly reducing the silicon layer thickness. In this study, we investigate two sets of samples. In the first set, the silicon layer thickness D is 15 nm and in the wavelength range from 12.4 nm to 14.0 nm have been measured for all samples at the EUV beamline at the MLS. The data obtained is shown in Fig. 4.7 sorted by the nominal molybdenum layer thickness. The reflectivity curves in Fig. 4.7 show the main broad maximum and side fringes, very similar to the mirror sample discussed in Sec. 4.1 above. In direct comparison of the measured reflectivity data, mirrors with a main broad maximum and side fringes, very similar to the mirror sample in Fig. 4.7a and Fig. 4.7b have the characteristic curve shape of periodic EUV multilayer structures with a main broad maximum layer thickness. The reflectivity curves measured for all samples at the EUV beamline at the MLS. The data obtained is shown normal of $a_i = 15^\circ$ and in the wavelength range from 12.4 nm to 14.0 nm have been spectrally resolved EUV reflectivity curves at an angle of incidence from the surface shifts of the peak center position are clearly visible. As illustrated in Fig. 4.4 above,

values of the molybdenum layers in the two sample sets are listed in table 4.4.

Period to counteract the possible roughening due to the crystallization. The nominal period during deposition, an additional polishing process was used once during sputtering each sputtered layers were deposited one after another for each sample. In the second set, sputtered layers were deposited two sets of samples. In the first set, the magnetron thickness. In this study, we investigate two sets of samples. In the second set, the silicon layer period thickness D thickness D is 7 nm constant by correspondingly reducing the silicon layer with increasing relative Mo thickness from sample to sample while keeping the nominal period thickness D is 7 nm constant by correspondingly reducing the silicon layer thickness. In this study, we investigate two sets of samples. In the first set, the silicon layer thickness D is 15 nm and in the wavelength range from 12.4 nm to 14.0 nm have been measured for all samples at the EUV beamline at the MLS. The data obtained is shown in Fig. 4.7 sorted by the nominal molybdenum layer thickness. The reflectivity curves in Fig. 4.7 show the main broad maximum and side fringes, very similar to the mirror sample in Fig. 4.7a and Fig. 4.7b have the characteristic curve shape of periodic EUV multilayer structures with a main broad maximum layer thickness. The reflectivity curves measured for all samples at the EUV beamline at the MLS. The data obtained is shown normal of $a_i = 15^\circ$ and in the wavelength range from 12.4 nm to 14.0 nm have been spectrally resolved EUV reflectivity curves at an angle of incidence from the surface

4.2.1 Sample systems and experimental procedure

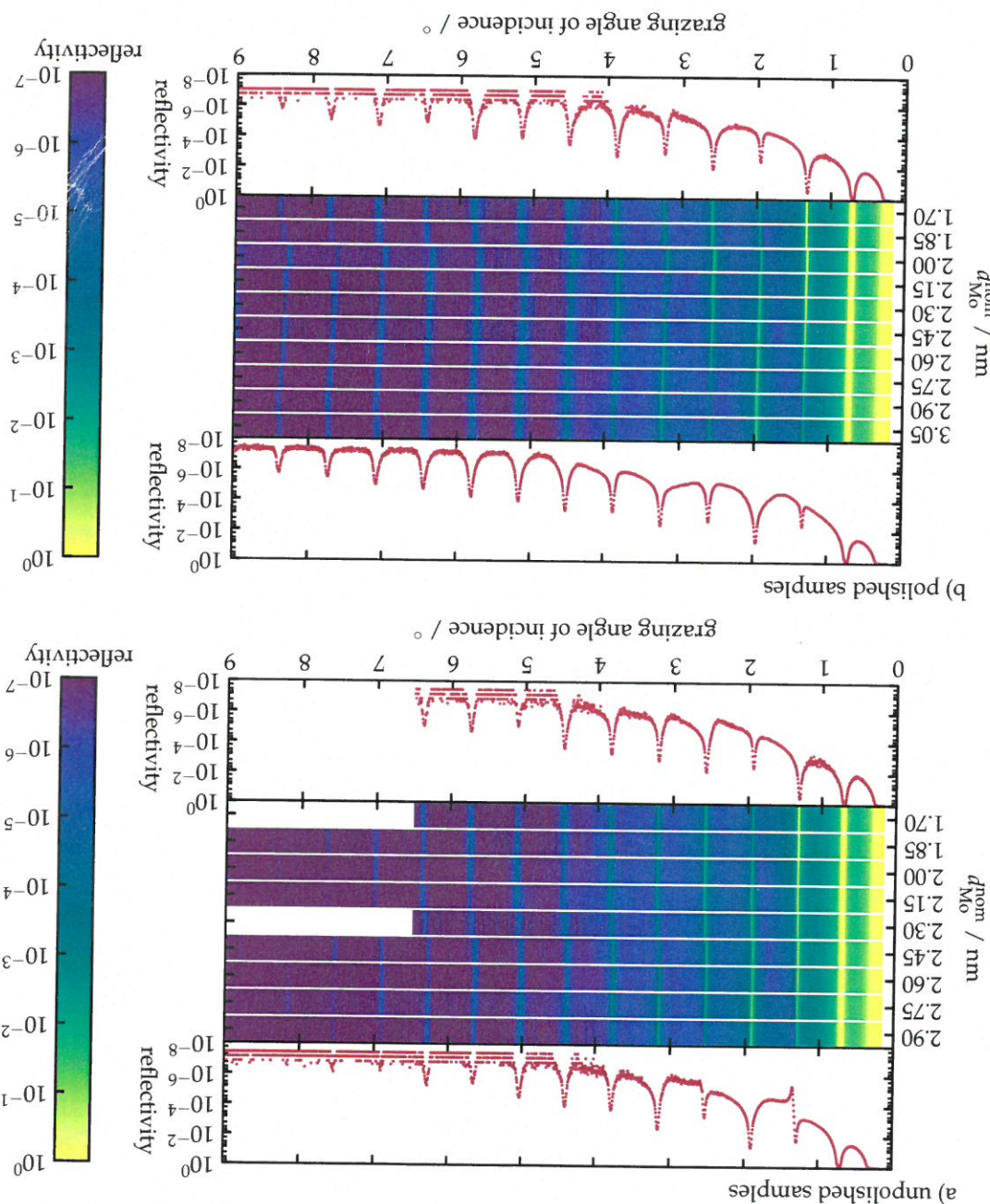
The goal of this investigation is to analyze the interface morphology in each sample and assess the effect of the crystallization process and the polishing treatment. For that, the nominally deposited layer thicknesses are verified and the model including the determination of the densities and the interdiffusion parameters is reconstructed in Sec. 4.2.2 based on specular analytical experiments and roughness measurements is determined with the PSD and the MCMC methods introduced above. The findings are shown and discussed in Sec. 4.2.3. The results presented here are part of the publication of the model for those samples is given below in Fig. 4.9 of the following sections) were of the model for the Mo on Si interfaces (a detailed figure of the model for those samples is given below in Fig. 4.9 of the following sections) were prepared. As mentioned above, the samples under investigation here were fabricated with increasing relative Mo thickness from sample to sample while keeping the nominal period thickness D thickness D is 7 nm constant by correspondingly reducing the silicon layer thickness. In this study, we investigate two sets of samples. In the first set, the silicon layer period thickness D is 7 nm constant by correspondingly reducing the silicon layer thickness. In this study, we investigate two sets of samples. In the first set, the silicon layer period thickness D thickness D is 15 nm and in the wavelength range from 12.4 nm to 14.0 nm have been measured for all samples at the EUV beamline at the MLS. The data obtained is shown in Fig. 4.7 sorted by the nominal molybdenum layer thickness. The reflectivity curves in Fig. 4.7 show the main broad maximum and side fringes, very similar to the mirror sample in Fig. 4.7a and Fig. 4.7b have the characteristic curve shape of periodic EUV multilayer structures with a main broad maximum layer thickness. The reflectivity curves measured for all samples at the EUV beamline at the MLS. The data obtained is shown normal of $a_i = 15^\circ$ and in the wavelength range from 12.4 nm to 14.0 nm have been spectrally resolved EUV reflectivity curves at an angle of incidence from the surface

scattering. In: *Optics Express* (2017).

Two sets of several samples of Mo/Si/C multilayer mirrors with C interdiffusion barriers with thicknesses of nominally below 0.5 nm at the Mo on Si interfaces (a detailed figure of the model for those samples is given below in Fig. 4.9 of the following sections) were prepared. As mentioned above, the samples under investigation here were fabricated with increasing relative Mo thickness from sample to sample while keeping the nominal period thickness D thickness D is 7 nm constant by correspondingly reducing the silicon layer thickness. In this study, we investigate two sets of samples. In the first set, the silicon layer period thickness D thickness D is 15 nm and in the wavelength range from 12.4 nm to 14.0 nm have been measured for all samples at the EUV beamline at the MLS. The data obtained is shown in Fig. 4.7 sorted by the nominal molybdenum layer thickness. The reflectivity curves in Fig. 4.7 show the main broad maximum and side fringes, very similar to the mirror sample in Fig. 4.7a and Fig. 4.7b have the characteristic curve shape of periodic EUV multilayer structures with a main broad maximum layer thickness. The reflectivity curves measured for all samples at the EUV beamline at the MLS. The data obtained is shown normal of $a_i = 15^\circ$ and in the wavelength range from 12.4 nm to 14.0 nm have been spectrally resolved EUV reflectivity curves at an angle of incidence from the surface

In the following we shall apply and extend the reconstruction procedure discussed in the above section to the problem of multilayer sample systems deposited with varying molybdenum layer thicknesses from sample to sample. The samples discussed in this section were designed to investigate the impact of the crystallization on the performance of Mo/Si multilayer mirrors systems. Two sets of samples were fabricated. One with the standard magnetron deposition technique, which we shall refer to as *unpolished samples*. On Mo/Si multilayer mirrors systems, two sets of samples were fabricated. One with the standard magnetron deposition technique, which we shall refer to as *unpolished samples*. Consequently, the latter samples are referred to as *polished samples*. Both sets were deposited with nearly increasing molybdenum thickness across all periods from sample to sample. The details of the sample layout and the reflectivity measured from each sample are described in detail in Sec. 4.2.1.

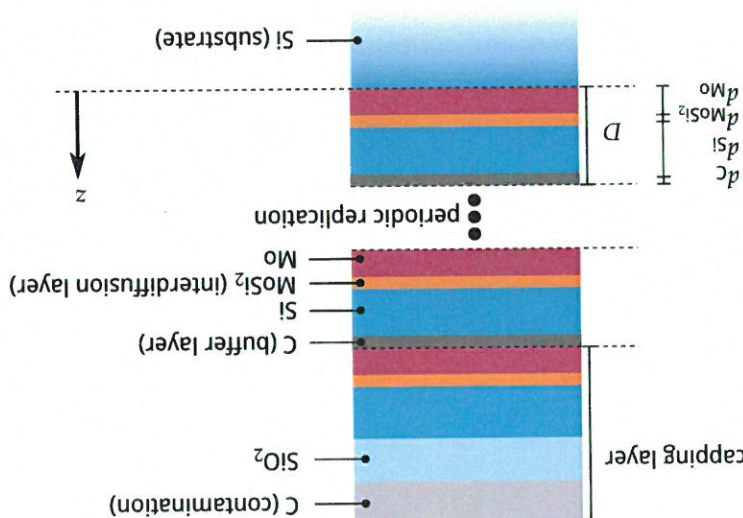
Figure 4.8 | XRR data for all unpolished and polished samples shown in dependence on the nominal molybdenum layer thickness d_{Mo} and the grazing angle of incidence α_{GI} at the Cu-K α photon energy of $E_{\text{ph}} = 8048 \text{ eV}$. In each of the subfigures a) and b) the top of the subfigure, respectively, shows the XRR curves are shown in as a color map plot. The XRR curves are shown on the bottom of the subfigure and the bottom of the top plot. In between, the and largest d_{Mo} are shown on the bottom and the top of the subfigure, respectively. In between, the sample with smallest d_{Mo} is shown on the bottom and the top of the subfigure, respectively. In between, the sample with smallest d_{Mo} is shown on the bottom and the top of the subfigure, respectively.



Parameter	Definition	Lower bound	Upper bound
d_{Mo} / nm	Mo layer thickness	0.0	4.5
d_{Si} / nm	Si layer thickness	0.0	7.0
d_C / nm	C buffer layer thickness	0.0	0.6
d_{MoSi_2} / nm	MoSi ₂ interdiffusion layer thickness	0.0	0.6
θ / nm	Nevo-t-Croce parameter	0.0	0.5
p_{Mo}	Mo density wrt. bulk density (identical for all interfacess)	0.8	1.0
p_{Si}	Si density wrt. bulk density	0.8	1.0
p_C	C density wrt. bulk density	0.8	1.0
p_{MoSi_2}	MoSi ₂ density wrt. bulk density	0.8	1.0
$d_{SiO_2(cap)}$ / nm	Capping layer thickness	0.0	3.0
$d_{SiO_2(cap)}$	= p_{Si} (identical to Si density)	0.0	1.0
$p_{SiO_2(cap)}$	$p_{SiO_2(cap)}$		

Table 4.5 | Parameterization of the Mo/Si/C multilayer samples with varying molybdenum layer thick-

Figure 4.9 | Model of the multilayer stack including the substrate and the capping layers. The periodic part is enclosed between the dashed lines with four layers in each period repeated 49 times. The capping period does not include an intermediate layer but has a silicon layer and a natural SiO_2 layer and a carbon-like layer acting as a counter for contamina-



CHARACTERIZATION OF THE MULTILAYER STRUCTURE FOR DIFFERENT SYSTEMS

for all parameters. An unambiguous result was only found with respect to the thicknesses. As a first step, the MCMC procedure was performed within the defined boundaries causes the confidence intervals to be different for the respective parameters.

Only distinction of broader or even improved distributions in some cases. The latter to show the same properties and the same findings discussed in the following with the results of the MCMC maximum likelihood estimation for the other samples were found unpollished sample with nominal molybdenum layer thickness of $d_{\text{Mo}} = 3.05 \text{ nm}$. The We shall discuss the results of the optimization procedure at the example of the parameter.

resulting from the MCMC as one standard deviation of the sample distribution in each each value within the underlying model are estimated from the likelihood distribution chosen in reference to prior knowledge and physical plausibility. Confidence intervals for is generated with respect to predefined boundaries listed in table 4.5. The limits are the procedure above in Sec. 4.1.2. As a starting point, again a random set of parameters the optimization result, although slower in convergence, as mentioned in the discussion of the decreased amount of layers and interfaces. The MCMC method itself yields start with a PSO optimization, since the sample system is numerically simpler due to MCMC method as described above for the Mo/B₄C/Si/C sample system. We do not To minimize the functional with respect to the best choice of parameters, we apply the conducted by minimizing the χ^2 functional (or equivalently maximizing the likelihood). The solution to the inverse problem of reconstructing the optimal model parameters is above. The combined χ^2 functional enters the likelihood through Eq. 4.4.

experiments, similarly to the procedure for a single EUV curve as described in Sec. 4.1 which represent a conservative (upper limit) estimation for the combined analysis of both we are therefore enabled to obtain confidence intervals for the parameters of the model,

$$\chi^2 = \chi_{\text{EUV}}^2 + \chi_{\text{XRR}}^2, \quad (4.6)$$

reduced to a single comparable quantity. By the definition of the squared residuals of model prediction and experiment. Thereby, each experiment is for each of the datasets separately. The reduced χ^2 can be interpreted as the average of

$$\chi^2 = \frac{1}{M-p} \left[\sum_m (I_{\text{model}}^m - I_{\text{meas}}^m)^2 \right], \quad (4.5)$$

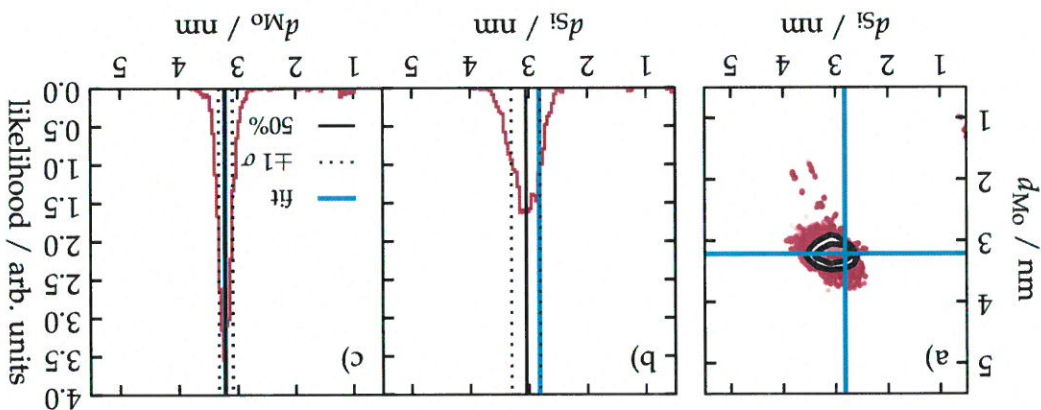
sum of the reduced χ^2 functionals. The χ^2 is equivalently defined to Eq. (4.1) through, fewer EUV data points. To avoid this effect, we define the combined χ^2 functional as the unwanted weighting due to the large amount of XRR data points in comparison to far point residuals, i.e. both the EUV data and the XRR data would therefore create an due to systematic errors. Defining a χ^2 functional as the total sum of all measured data data points, e.g. by reducing the angular step size by half does not lead to better statistics entirely independent of each other. In case of the XRR curve increasing the number of XRR reflectivity curves have significantly different number of data points, which are not required to allow an analysis based on both data sets. The two data sets, i.e. the EUV and through the additional XRR measurements, a definition for a combined χ^2 functional is the goal to improve the reconstruction of the model. Due to the increased amount of data for the samples studied here, two separate experiments and data sets were measured with The data analysis was conducted similarly to the procedure described in Sec. 4.1. However,

Optimization functional and procedure

In a second step, another MCMC optimization was performed on a reduced parameter set, fixing the determined molybdenum layer thickness to its optimal value, i.e. the 50% percentile of its distribution. Finally, the layer thicknesses of the C barrier layer and the MoS₂ interdiffusion layer were fixed to their nominal values of $d_C = d_{\text{MoS}_2} = 0.5 \text{ nm}$. Due to the broad distribution result for the likelihoods of those parameters, this comes without a limitation of the generality for this analysis, since any value is valid within the predefined boundaries. Additionally, this ensures comparability of the models for all samples without constraining the applicability of the model with respect to the data.

the inclusion of additional XRR measurements lead to significantly smaller confidence intervals and thus higher accuracy of the reconstruction. The method of combining the analysis of two datasets of EUV and XRR measurements has been previously applied by others [13], which have come to the same result of a significantly improved model reconstruction. Each of the methods does provide different sensitivity for the different model parameters. As an example, EUV measurements are sensitive to the Mo and Si layer thicknesses due to the large optical contrast in that spectral range. On the other hand, high accuracy can be expected from the XRR measurements with respect to the layer thicknesses due to the large optical contrast in that spectral range.

Figure 4.10 | Results of the maximum likelihood estimation obtained via the MCMC procedure similar to Fig. 4.5 but for the combination of EUV and XRR data. a) Two dimensional projection of the likelihood distribution for the parameter pair d_1 and d_0 . The projection was obtained by marginalizing over all other parameters of the model. The black contours indicate the areas for one and two standard deviations (one and two sigma contours). The blue lines in all three sub-figures indicate the best parameter set found with the 50 nm method; b) One dimensional projection of the likelihood distribution for the silicon layer thickness d_1 . The solid black line marks the center position (50% percentile) of the distribution. The dotted lines are the limits of one standard deviation. c) The one dimensional distribution of the molybdenum layer thickness.



parameters of Mo, with the smallest confidence intervals in comparison to all other parameters, and Si, as well as for the Nevo-Croce parameter α , whereas all other parameters show broad likelihood distributions within the predefined boundaries not allowing a unequivocal parameter determination. Therefore, the best model was obtained in a two-step process. First the MCMC optimization was performed including all parameters as mentioned above. Proceeding from this, the value of the Mo thickness with its confidence interval was obtained by marginalizing over all other parameters, yielding the most precise parameter estimation from the Mo/Si/C/B₄C system.

The optimal parameters for the molybdenum layer thickness d_{Mo} and the period

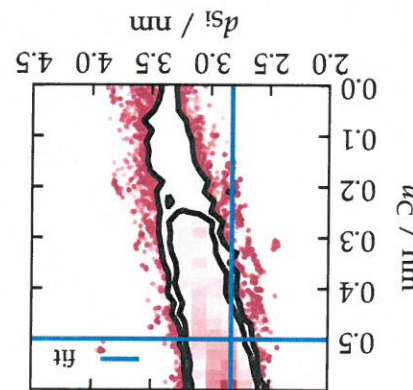
nom. d_{Mo} / nm	EUV & XRR (unpolished)	EUV & XRR (polished)	Table 4.6 List of nom-
1.70	1.81(-0.12/+0.24)	1.77(-0.22/+0.19)	final molybdenum layer-
1.85	1.98(-0.15/+0.14)	1.91(-0.12/+0.17)	thicknesses in the two
2.00	2.08(-0.11/+0.22)	2.29(-0.28/+0.13)	sample sets. Both sets
2.15	2.31(-0.022/+0.21)	2.45(-0.43/+0.06)	were fabricated with a
2.30	2.43(-0.09/+0.16)	2.60(-0.12/+0.14)	equidistant increase in
2.45	2.68(-0.13/+0.16)	2.58(-0.21/+0.15)	thickness from 1.70 nm
2.60	2.91(-0.17/+0.12)	2.87(-0.22/+0.12)	to 3.05 nm with 9 unpol-
2.75	3.02(-0.15/+0.15)	3.03(-0.16/+0.14)	ished and 10 polished
2.90	3.22(-0.13/+0.11)	3.15(-0.13/+0.13)	samples.
3.05	-	3.47(-0.19/+0.13)	

experimental values and their confidence intervals is given in table 4.6. The theoretical sample with $d_{Mo} = 3.05$ nm are shown in Fig. 4.12. Overall, a very good agreement of the two experiments with the theoretical curves is obtained. The full list for all nominal molybdenum layer thicknesses for all samples with the respective sample sets. Both sets were fabricated with a equidistant increase in thickness from 1.70 nm to 3.05 nm with 9 unpoltished and 10 polished samples.

4.2.3 Optimization results

The results of the second MCMC procedure of the restricted model yielded the remaining values for the model parameters by obtaining the globally best solution found. The final result is indicated by the blue solid lines in Fig. 4.10. Due to the choice to restrict the model to a buffer layer thickness of $d_C = 0.5$ nm, we find the optimal solution for the silicon layer thickness at the limit of one standard deviation for the silicon and carbon layers thicknesses are strongly correlated as shown in Fig. 4.10b. The distributions shown represent the MCMC results of the unrestricted model, where the silicon layer thickness at the limit of one standard deviation in Fig. 4.10b. The distributions show the MCMC results of the unrestricted model, where the silicon and carbon layers thicknesses to its nominal value, this correlation is resolved and the fixing the carbon layer thickness is well within the interval of one standard deviation corresponding silicon layer thickness is well within the interval of one standard deviation as indicated through the solid black contours in Fig. 4.11.

Figure 4.11 | Two-dimensional likelihood distribution indicating the correlation of the remaining parameters over all marginalizing over all of the model. The blue lines indicate the fit obtained through the two-step MCMC optimization procedure (see main text).



available.

accordingly. In both cases, a significant dip with respect to the expected value can be observed roughlyness/interridiffusion to the model and varying the molybdenum thickness maximum peak reflectance values for the two sample systems calculated by adding the of $d_{SiO_2} = 2.0$ nm was considered. The dashed curves in both figures show the expected layer of $d_{cap} = 2.0$ nm and a relative density of $P_{(cap)} = 0.5$ and a silicon dioxide layer thickness without any interdiffusion or roughness. For the calculation, a carbon capping peak reflectance of all EUV measurements as a function of the reconstructed Mo layer thickness. The identical blue solid line in both subfigures indicates the maximum polished set. To better understand this observation, Fig. 4.14 shows the maximum peak reflectance of all EUV measurements for the polished samples and between $d_{Mo} \approx 2.3$ nm and $d_{Mo} \approx 2.7$ nm for the 2.3 nm for the polished samples and between $d_{Mo} \approx 1.9$ nm and $d_{Mo} \approx 2.7$ nm for the For both sets, distinct jumps can be observed between $d_{Mo} \approx 1.9$ nm and $d_{Mo} \approx$ fitted molybdenum thicknesses.

described. In Fig. 4.13b the fitted period thicknesses D are shown in dependency of the Thus, the nominal amount of deposited molybdenum leads to higher thicknesses than state, leads to density reduced layers compared to fully crystalline bulk molybdenum. the magnetron sputtered Mo layer, which is in mostly amorphous or polycrystalline density values of $P_{Mo} \approx 90\%$ w.r.t. the Mo bulk density. It is reasonable to assume, that found in the reconstruction results for all samples showing systematically reduced molybdenum density. The reduced relative density of the molybdenum layer is indeed of the molybdenum layer with the model reconstruction results, is the possible interdiffusion observation, consistent with the nominal values. A possible cause for that a systematically higher thickness than the nominal values. However at results show the desired linear increase in molybdenum layer thickness, however i.e. for the unrestricted model with the parameter limits as listed in table 4.5. The likelihood determined for the Mo layer thickness by the first-step MCMC procedure, Fig. 4.13. The confidence intervals shown in Fig. 4.13a are one standard deviation of thickness D found for both sample sets in the two-step MCMC analysis are shown in

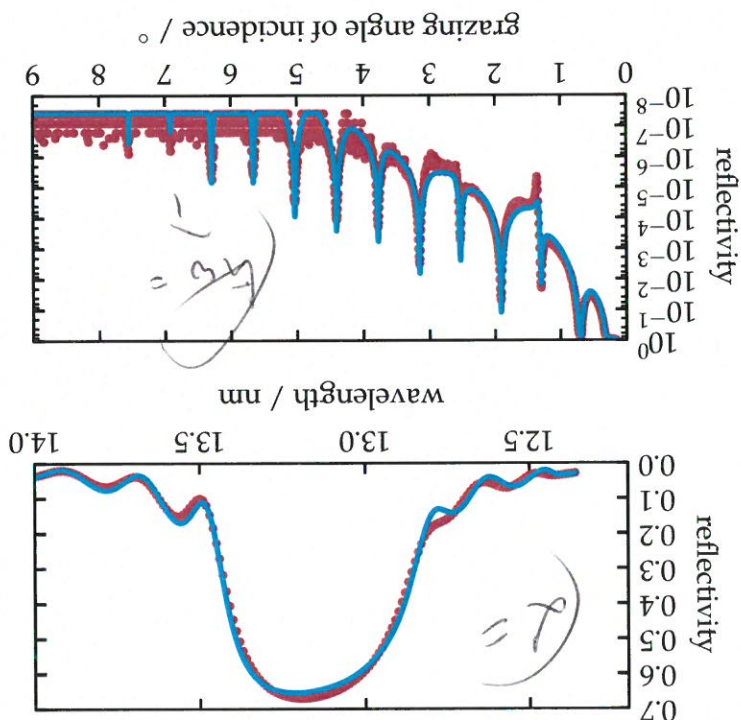


Figure 4.12 | Experimental data in comparison with the theoretical calculation of the model parameters obtained from the combined XRR data. The binned analysis of EUV obtained from the comparison of the model calculated with the theoretical curves with the experimental data shown here was measured on the unpolished sample with nominal thickness of $d_{Mo} = 3.05$ nm. final molybdenum thickness of $d_{Mo} = 3.05$ nm.

The reflectivity of the sample in the water window spectral range from 3.12 nm to 3.16 nm was measured at the soft x-ray beamline (SX700) beamline at electron storage ring for synchrotron radiation (BESSY II). The angle of incidence was $\alpha_i = 1.5^\circ$ (corresponding to $\lambda = 3.16 \text{ nm}$)

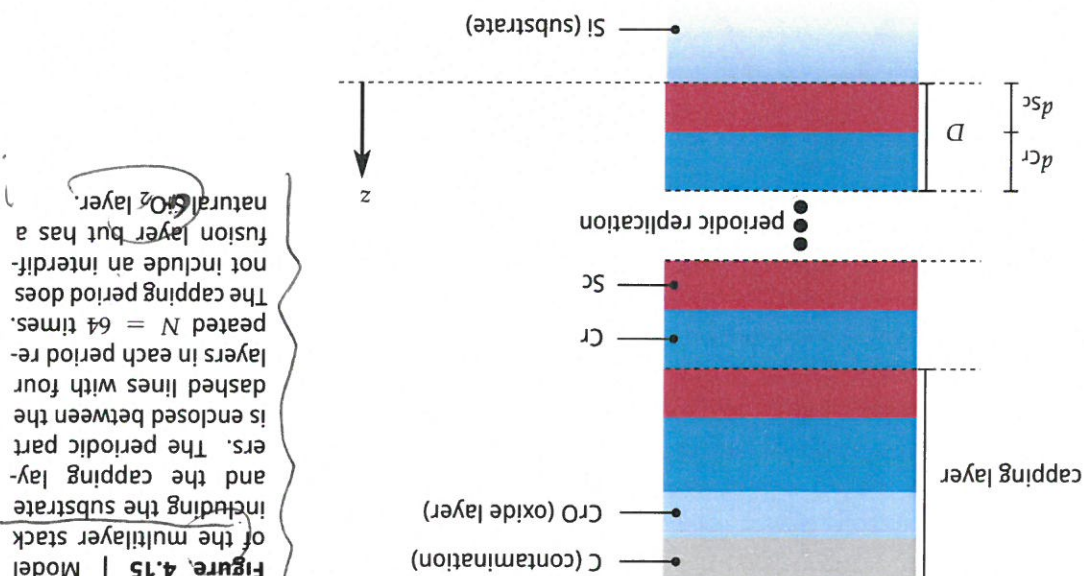
Parameter	Definition	Lower bound	Upper bound
Capping Layer			
dC / nm	Cr layer thickness	0.0	1.5
dSc / nm	Sc layer thickness	0.0	1.5
a / nm	Nevoit-Croce parameter	0.0	0.5
pCr	Cr density w.r.t. bulk density (identical for all interfaces)	0.5	1.0
pSc	Sc density w.r.t. bulk density	0.5	1.0
$dCr(\text{cap}) / \text{nm}$	SiO ₂ capping layer thickness	0.0	3.0
$dSc(\text{cap}) / \text{nm}$	SiO ₂ capping layer thickness	0.0	1.5
$pCr(\text{cap})$	Cr (cap) density w.r.t. bulk density	0.5	1.0
$pSc(\text{cap})$	Sc (cap) density w.r.t. bulk density	0.5	1.0
Capillary			
$dC(\text{cap}) / \text{nm}$	C capillary thickness	0.0	1.0
$dSc(\text{cap}) / \text{nm}$	Sc capillary thickness	0.0	1.0
$pC(\text{cap})$	C density w.r.t. bulk density	0.0	1.0
$pCr(\text{cap})$	Cr density w.r.t. bulk density	0.0	1.0
$dCr(\text{cap}) / \text{nm}$	SiO ₂ capillary layer thickness	0.0	3.0
$dSc(\text{cap}) / \text{nm}$	Sc capillary layer thickness	0.0	1.5
$pC(\text{cap})$	C density w.r.t. bulk density	0.0	1.0
$pCr(\text{cap})$	Cr (cap) density w.r.t. bulk density	0.5	1.0

Table 4.7 | Parameterization of the Cr/Sc binary multilayer model.

In analogy to Sec. 4.2, we seek to reconstruct the individual layer thicknesses based on experimental data. For this we construct a discrete layer model as illustrated in Fig. 4.15 in analogy to the procedure applied for the Mo/Si multilayer systems. The parameters of this discrete layer model are listed in table 4.7 together with the upper and lower bound for the particle swarm optimization procedure.

4.3.1 Reconstruction with a discrete layer approach

limit to the applicability of discrete layer models.

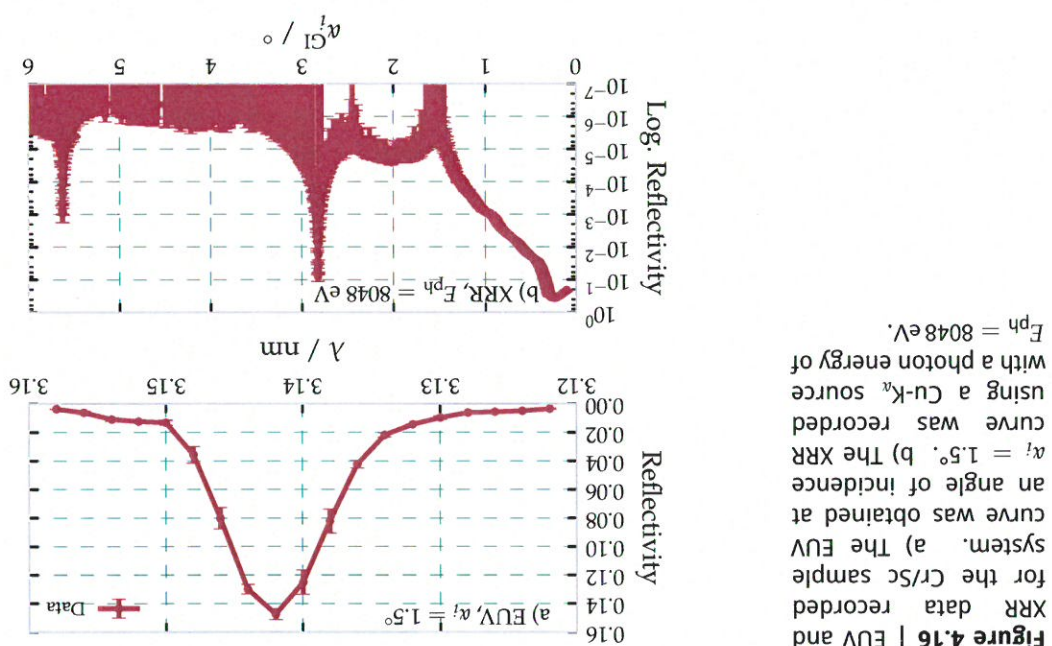


Analysis of Cr/Sc Multilayers with Sub-nanometer Layer Thickness

To better illustrate the differences to the Mo/Si systems, we have conducted an analysis based on the discrete layer model of a Cr/SC multilayer as described above. The particle swarm optimization was done based on the EUV data shown in Fig. 4.16a and the parameters and limits listed in table 4.7. The resulting parameters are listed in table 4.8.

In comparison, the most remarkable difference with respect to the Mo/Si mirrors is the significantly reduced measured peak reflectance of the EUV curve in Fig. 4.16a compared to the curves in Fig. 4.1 and Fig. 4.14. The maximum experimental value attained is only approximately $R_{\text{max}} \approx 15\%$ while it is up to $R_{\text{max}} \approx 70\%$ for the Mo/Si systems.

multilayer sample, only two Bragg peaks could be observed in this angular range in the XRR curve. All expected higher order peaks were below the detection threshold of 10^{-6} in reflected intensity. The dominating experimental uncertainty was the inhomogeneity of the sample stack across the sample area. The given uncertainty values for each of the measurement points were estimated, by measuring the peak reflectance of the EUV reflectivity curve at positions marking a cross of 2 mm by 2 mm in the sample centre. This data was compared to theoretical expectation value based on a PSO fit of the discrete layer model above (for details of the optimization results see below). From this a discrete difference of two theoretical curves attaining the maximum and minimum D values. Similarly, uncertainties for the XRR curve were calculated by simulating theoretical curves based on the same period drifts.



Both measurement curves are shown together in Fig. 4.16. Due to the short period of the grazing angle of incidence of $\alpha_i = 88.5^\circ$, which corresponds to the design goal for this mirror prototype. In addition, similar to the Mo/Si samples, a XRR measurement was conducted in the DESY laboratory using a laboratory-based X-ray diffractometer (XPert PRO MRD, Panalytical). The diffractometer is equipped with a high-resolution goniometer and uses Cu-K α radiation as a source. The XRR intensities were recorded using a PIXcel counting detector. The dynamic range achieved in the measurements extended down to a reflectance of 10^{-6} for grazing angles of incidence of $\alpha_i = 0^\circ$ to $\alpha_i = 3^\circ$.

maximum reflectance (cf. Fig. 4.14), hints at strong roughness or intermixing of the two especially compared to Mo/Si systems which are very close to the theoretically achievable above, theoretical reflectance values of $R_{\max} > 50\%$ are possible. This large difference, to the theoretically achievable maximum reflectance. For the particular model derived curve shows excellent agreement with the measured data, there is a significant offset (r.m.s.) value of $\sigma = 0.385 \text{ nm}$ for the Nevoit-Croce factor. While the EUV reflectance (S_C) to Cr ratio was found to be $T_{S_C} = d_{S_C}/d_{Cr} = 0.48$ with a root mean square in table 4.8, but without any roughness or interdiffusion, i.e. by requiring $\sigma \equiv 0.0$. was obtained by calculating the resulting reflectivity based on the parameter results

without any roughness or interdiffusion.
system without rough-
ing a perfect multilayer-
ical reflectance assum-
the maximum theoret-
The green curve shows
on the binary model.
1.5° from normal, based
action implying that $\alpha_i =$
wavelength of the radi-
ance curves across the
and XRR data excluding the areas of the Bragg peaks. This grazing incidence reflectivity
from an EUV curve alone as demonstrated in Sec. 4.1.

The theoretical curve obtained from the PSO procedure is shown in Fig. 4.17 in direct comparison with the theoretically achievable maximum reflectivity curve. The latter

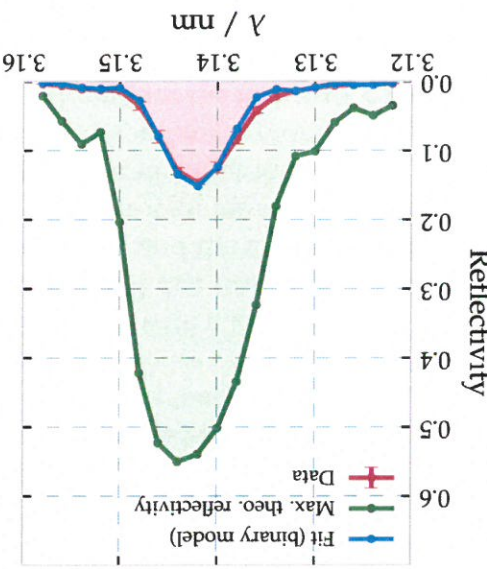


Figure 4.17 | Fitted ex-

perimentlal EUV reflect-
ance across the wave-
length of the radi-
ation implying that $\alpha_i =$
the maximum reflectiv-
ity for the top surface layers, which can not be deduced
and XRR data excluding the areas of the Bragg peaks. This grazing incidence reflectivity

Parameter	PSO result	PSO fit res-
d_{Cr} / nm	0.8224	0.8224
d_{S_C} / nm	0.7510	0.7510
σ / nm	0.375	0.375
p_{Cr}	0.876	0.876
p_{S_C}	0.957	0.957
Capping Layer		
d_C / nm	0.462	0.462
$d_{Cr}(\text{cap}) / \text{nm}$	1.143	1.143
$d_{S_C}(\text{cap}) / \text{nm}$	2.322	2.322
$p_C(\text{cap})$	0.502	0.502
$p_{Cr}(\text{cap})$	0.618	0.618
$p_{CrO}(\text{cap})$	0.851	0.851

Table 4.8 | PSO fit res-

The capping layer results were obtained in a combined PSO analysis based on the EUV

The physical structure of Cr/Sc multilayer systems with individual layer thicknesses in the sub-nanometer regime is significantly different than in case of the comparable large thicknesses of several nanometers in the Mo/Si systems. It is well known [84], that magnetron sputtered Cr and Sc multilayer systems, similarly to the Mo/Si systems, suffer from imperfect interfaces. Phase diagrams of Cr/Sc systems show, that the two materials do not like to mix or form composites at the interfaces [19]. That makes them an ideal candidate for chemically abrupt multilayer structures as needed for multilayer mirrors. However, due to the very thin layer structure, both

4.3.2 Extending The Model to Graded Interfaces and Interdiffusion

layer properties compared to the Mo/Si sample systems above.

Introducing additional parameters to account for the increased complexity of the samples does not suffice to describe the sample. Therefore, a more elaborate model is required due to the complementary data delivered through the measurement observations, mostly peak of the XRR curve. This is a strong indicator, that the simple model as defined above does not suffice to describe the sample. In a strict binary model like this one with a layer thickness ratio of $T_{Sc} \approx 0.5$, the second Bragg peak is additively suppressed due to symmetry reasons. Thus, there is a clear mismatch of the model reconstruction and the experimental observations, mostly due to the complementary data delivered through the measurements, mostly second Bragg peak is additively suppressed due to symmetry reasons. The curve in the XRR does not be brought into agreement with the existence of the second Bragg peak in the XRR. A fully combined analysis of the measured level could be required to reduce the theoretical EUV reflectance down to the measured value of approximately 10^{-3} is not represented by the model at all. A fully combined analysis of the second Bragg resonance, clearly visible with a peak reflectance value of only the first Bragg peak is found to be matched by the model also in the X-ray regime. Again, the EUV data is matched rather good, while in the case of the XRR measurement only the first Bragg peak is matched by the model used here, the X-ray regime.

Figure 4.18 | a) Measured EUV reflectivity curve for the near-normal angle of incidence of $\alpha_i = 1.5^\circ$. Together with the theoretical curve based on the PSD optimized binary multilayer model. b) Measured and calculated XRR curves for the same sample and model parameters at grazing angles of incidence using radiation at the Cu-K α wavelength. A clear mismatch of the theoretical curve and the measured data can be observed for the second Bragg peak between $\alpha_f = 5.0^\circ$ and $\alpha_f = 6.0^\circ$.

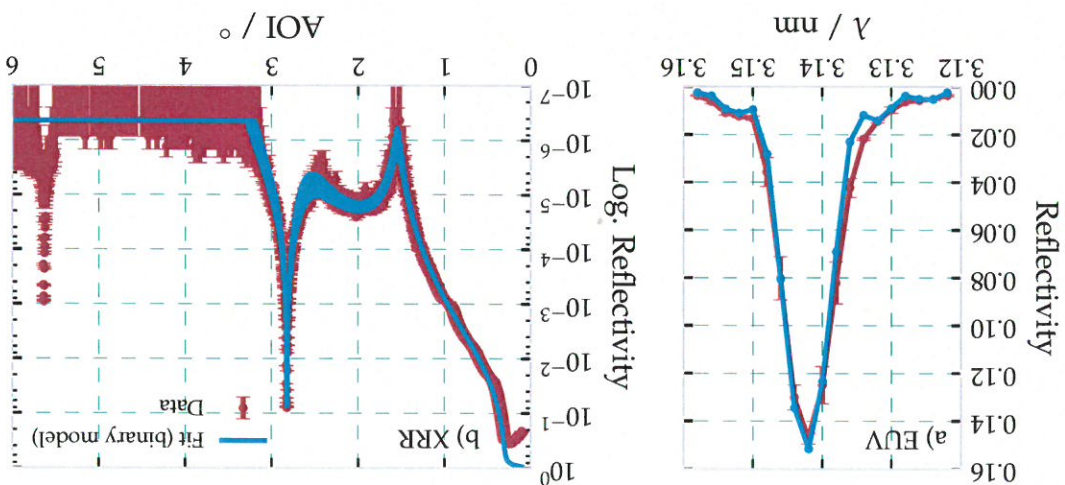
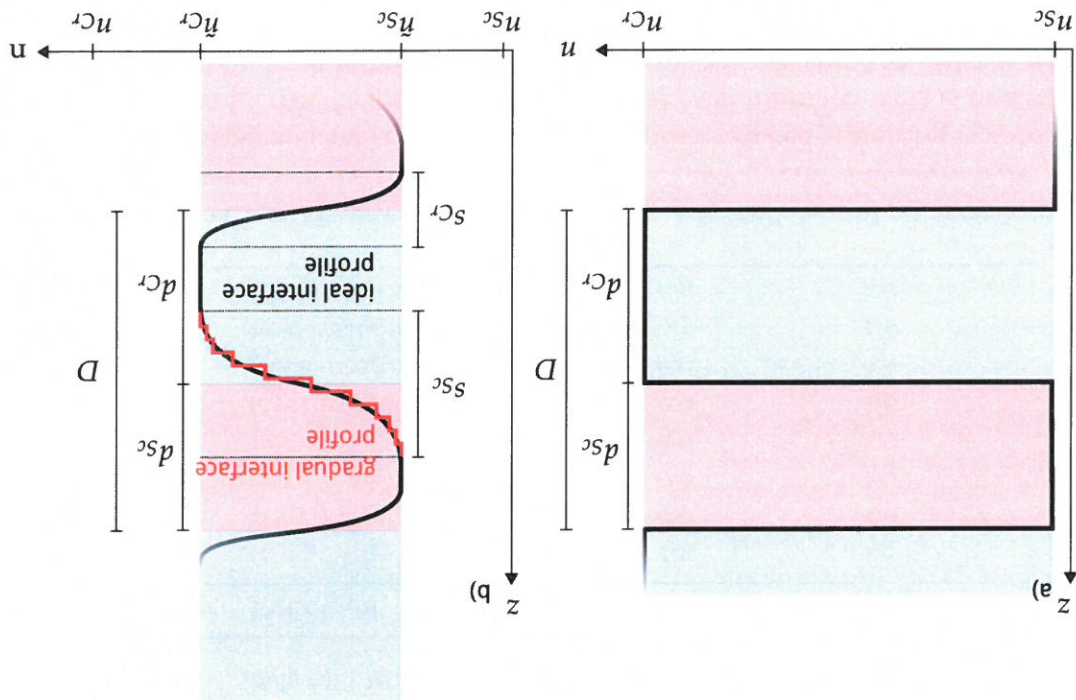


Fig. 4.18. Calculated curves for both experiments, the EUV and XRR curve, are shown together in materials. To verify the applicability of the discrete (binary) layer model used here, the calculated curves for both experiments, the EUV and XRR curve, are shown together in Fig. 4.18.

FIGURE 4.19 | a) Binary Cr/Sc multilayer model with total period thickness D and the individual layer thicknesses d_{Sc} and d_{Cr} . The effective index of refraction for both layers is given by n_{Sc} and n_{Cr} , respectively. **b)** Model with discrete sublayers as indicated in red, forming the actual gradual interface profile is approximated through the electric field calculations in red, forming a sinusoidal profile. The total thicknesses are given by n_{Sc} and n_{Cr} . The interdiffusion zones can differ for the top and bottom interface in each period. Their total thicknesses are given by s_{Sc} and s_{Cr} . The ideal interface profile is shown in black, while the actual profile is shown in red.



to the simple model used before. The interdiffusion zones are modeled following Cr/Sc multilayer sample measured above is illustrated in Fig. 4.19 in direct comparison if the interdiffusion zones are asymmetric. The model, which we use to reconstruct the Bragg peak is no longer suppressed even though both layers have the same thickness depending on whether Cr was deposited on Sc or vice versa. Thereby, the second this symmetry effect can be broken by interdiffusion zones with different thicknesses, above leads to a suppression of the second order Bragg peak. Nevertheless, physically above symmetry of two identically thick layers within one period in the simple model possible interdiffusion gradients and intermixing between the two materials in the stack. a more complex model is required. Here, we define a periodic model to account for parameter α does not provide an accurate model with only a Nevo-Croce damping shown above, clearly demonstrate that a binary model with XRR measurements total layer thickness itself. The results from the specular EUV and XRR radiation of $\alpha = 3.14 \text{ nm}$, roughness and interdiffusion may occur over a zone as large as the required to achieve the first Bragg resonance upon near-normal incidence with radiation abrupt transition from one material to the next. Due to the small layer thicknesses addition, roughness at the interfaces exists and further diminishes an ideal chemically sputtering deposition, which has shown to cause intermixing upon deposition [38]. In structures similar to the one discussed here [44]. Another possible reason is the magnetron materials are in an amorphous state and intermixing was in fact observed for multilayer

thicknesses of the Cr and Sc layers as indicated in Fig. 4.19, and p_{Sc} and p_{Cr} , their respective densities with respect to their bulk densities $\rho_{Sc} = 2.989 \text{ g/cm}^3$ and $\rho_{Cr} = 7.19 \text{ g/cm}^3$ [53]. The loss of specular reflectance due to roughness-induced scattering is considered through the Nevo-t-Croce factor using q_f , identical at each interface. This is necessary to account for diffusely scattered light, which is missing in the measured specularity reflected radiation but can not be attributed to contrast loss due to interdiffusion. The parameter T_{Sc} indicates the portion of the Sc layer thickness with respect to the full period thickness D , which together uniquely define the thickness d_{Cr} . L_o describes the asymmetry of the widths of the interdiffusion zones at the Cr on Sc and Sc on Cr interfaces and is limited physically by the interval $L_o \in [0, 1]$. Note that s_{Sc} and s_{Cr} are half periods of the sinus functions used to describe the interface profiles. Therefore the condition $s_{Sc} + s_{Cr} \leq D$ holds.

Parameter	Definition	Lower bound	Upper bound
D / nm	$= dS_c + dCr$	1.5	1.6
T_{Sc}^c / nm	$= dS_c / D$	0.0	1.0
Sd / nm	$= SS_c + Sc_r$	0.0	1.6
T_s^c	$= SS_c / Sd$	0.0	1.6
Sc_r / nm	$= Sc_c + Sc_r$	0.0	1.0
d_r / nm	Layer intermixing r.m.s. roughness	0.0	1.0
ps_c	Sc density wrt. bulk density	0.5	1.0
pc_r	Cr density wrt. bulk density	0.5	1.0

Table 4.9 | Multilayer parameterization and parameter limits

With the definition of the model as outlined above, natural restrictions arise for the parameters. As an example, the interdiffusion zone region can not extend across half of the thickness of the original layers total thickness described by the parameter d_C , or d_S , respectively. Instead, the intermixing parameter would have to be increased to account for that situation. The model is therefore parameterized according to the list of effective parameters given in table 4.9 together with their allowed ranges for the optimization procedure in analogy to the analysis conducted in the previous sections. The range limits arise either from physical plausibility or are intrinsic properties of the parameter definition. Here, D is the full period thickness, d_S and d_C are the nominal layer

where n_C and n_S are the tabulated values [53] with densities p_C and p_S .

$$n_{\text{CR}} = (\eta/2)n_{\text{SC}} + (1 - \eta/2)n_{\text{C}^*}, \quad n_{\text{HS}} = (1 - \eta/2)n_{\text{SC}} + (\eta/2)n_{\text{C}^*}, \quad (4.7)$$

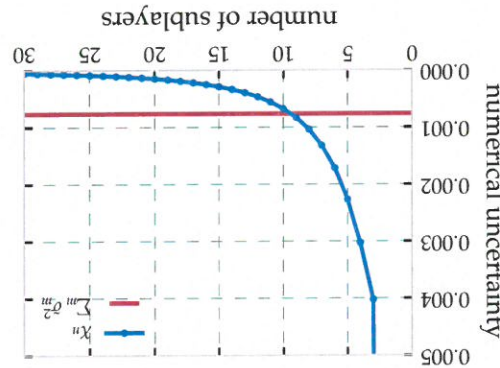
smooth transition from the refractive index of the Cr layer to the Sc layer and vice versa. The thicknesses of those zones is given by the parameters Sc_c and Cr_c . For the calculation of the electromagnetic fields inside the stack, the interface region is sampled with a fixed number of equally spaced points in z-direction, effectively creating a region of thin sublayers with a gradually changing index of refraction (illustrated by the red stepped function in Fig. 4.19). To take into account intermixing extending across the full period, we introduced an intermixing parameter η . The effective indices of refraction of the individual Cr and Sc layers are then given through

gradual interface model clearly provides a more accurate representation of the sample Based on the example of a combined analysis of EUV and XRR data in this section, the EUV curve.

of the XRR curve in Fig. 4.21d while also maintaining an excellent agreement with the significant improvement of the optimized result with perfectly match in both Bragg peaks which is shown once again in Fig. 4.21b. For the gradual interface model, we see a binary model, we have seen the distinct mismatch with the second order Bragg peak, as already found above and also the gradual model in Fig. 4.21a and Fig. 4.21c. For the EUV reflectivity curves show visually indistinguishable fits for both, the binary model and the gradual model are shown in direct comparison with each other in Fig. 4.21. The functional defined in Eq. (4.6). The results found for the binary model (cf. Fig. 4.18) approach is applied to obtain a global solution for the model parameters by minimizing described in Sec. 4.2.2 to the improved gradual model. The particle swarm optimization Fig. 4.16 above, we have applied the combined analysis technique for the two sets representing the physical structure that could describe the EUV and XRR data shown in As a verification of the applicability of the model to the problem of accurately rep-

only a marginal additional numerical error is acquired due to insufficient sampling. for all calculations. At that value, the experimental uncertainty is clearly dominant and the electromagnetic field for all measurements discussed here, we use $n = 15$ sublayers the analysis is this chapter, and due to reasons of numerical effort required to calculate uncertainties at the lower limit of $n = 10$ sublayers for the interface zone. For

Figure 4.20 | Numerical uncertainty
The numerical uncertainty of each data point in Fig. 4.16a, $\mathcal{L}_m^{(l,m)}$.
numerical uncertainty
gradual layer model in
duced through a coarse
initial uncertainty intro-
duced to all measurements
discussed here, we use $n = 15$ sublayers
the electromagnetic field for all measurements discussed here, we use $n = 15$ sublayers
the analysis is this chapter, and due to reasons of numerical effort required to calculate
uncertainties at the lower limit of $n = 10$ sublayers for the interface zone. For



with respect to the EUV reflectivity curve. As illustrated in Fig. 4.20, the experimental parameters used for this analysis were obtained through a PSO optimization of the model interfaces and an "ideal" smooth transition represented by 100 sublayers. The model of the difference of the theoretical EUV curves with increasing numbers of gradual

$$\chi_n = \sum_{m=100}^n (I_m - I_m^*)^2 \quad (4.8)$$

sublayers was evaluated by comparing the sum of squares The numerical error of the model depending on the interface sampling through gradual uncertainty of each data point in Fig. 4.16a, $\mathcal{L}_m^{(l,m)}$.

curve, which serves as a reference for this assertion through the sum of the squared accurate experiment of the analysis within this chapter is given by the EUV reflectivity this number, we have evaluated the mean error introduced by coarse sampling. The most required to reflect the physical situation of a smooth transition. To assert a lower limit for an additional numerical uncertainty through the number of discretization points n The discretization of the smooth interface profile in the interdiffusion zones introduces

Figure 4.21 | Comparison of the reconstructions of the binary and gradual models for the EUV and XRR data. a) Measured EUV reflectivity curve for and near-normal angle of incidence of $\alpha_i = 1.5^\circ$. Together with calculated curves for the same sample at the same Cu-K α wavelength. b) Measured and calculated XRR curves for the same sample and model parameters at grazing angles of incidence using radiation at the Cu-K α wavelength. A clear mismatch of the theoretical curve and the measured data can be observed for the second Bragg peak between $\alpha_i = 5.0^\circ$ and $\alpha_i = 6.0^\circ$. c) Measured EUV reflectivity curve for the second Bragg peak between $\alpha_i = 1.5^\circ$ and $\alpha_i = 1.5^\circ$ together with calculated curves for the same sample and model parameters at grazing angles of incidence using radiation at the Cu-K α wavelength. A clear mismatch of the theoretical curve and the measured data can be observed for the second Bragg peak between $\alpha_i = 5.0^\circ$ and $\alpha_i = 6.0^\circ$. d) Measured and calculated XRR curves for the same sample and model reconstruction at the Cu-K α wavelength.

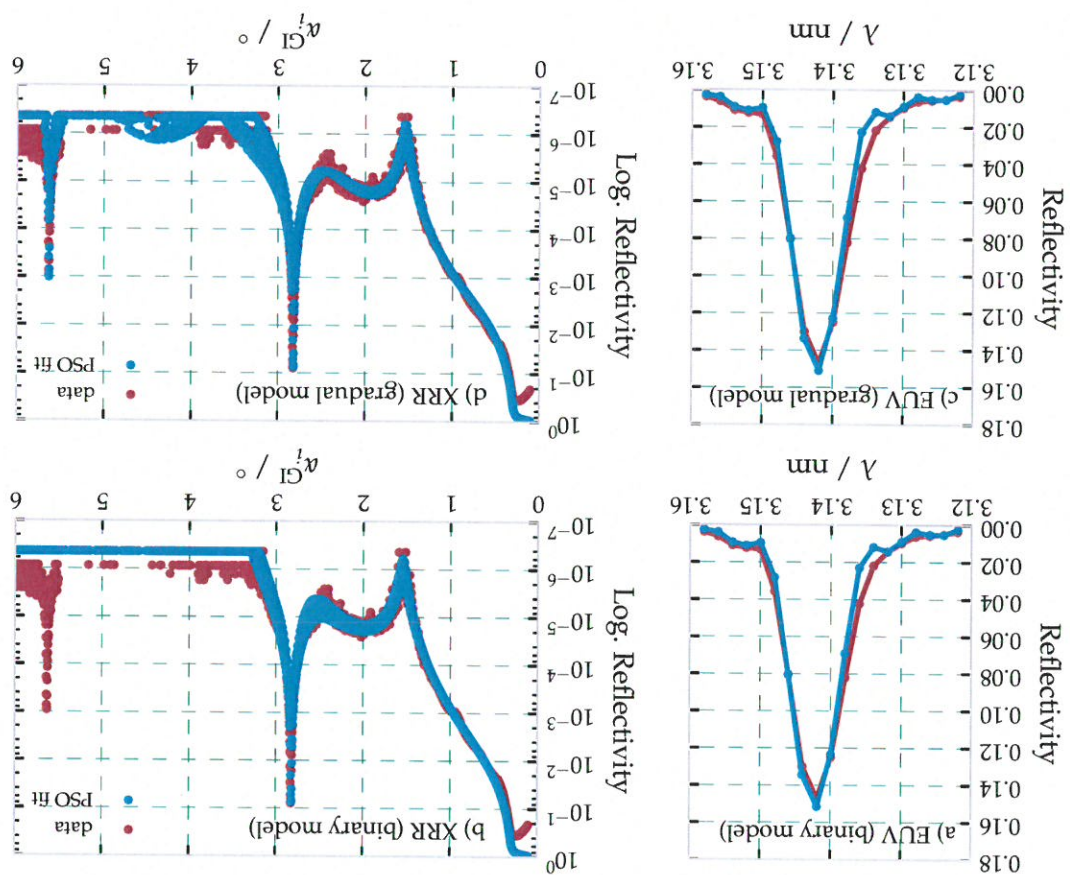
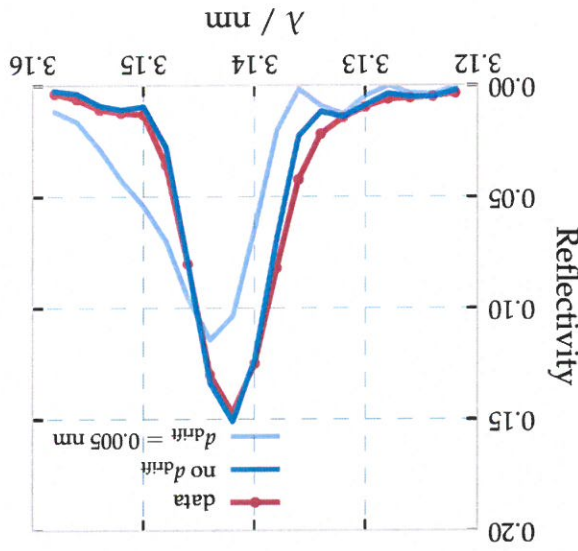


Figure 4.22 | EUV peak deformation assuming a constant drift of $a_{drift} = 0.005 \text{ nm across the total multilayer stack keeping the mean period thickness } D \text{ constant.}$



at $\lambda \approx 3.153 \text{ nm}$, which is not observed in the data.

peak symmetry with a significant minimum at $\lambda \approx 3.136 \text{ nm}$ and an additional shoulder at $\lambda \approx 3.153 \text{ nm}$, which is not observed in the data. This distortion is caused by a drift of the total period thickness D across the whole stack of $N = 400$ periods by $a_{drift} = 0.005 \text{ nm}$ based on the model parameters for the deposition process. Fig. 4.21 keeps the mean period thickness constant. Clearly, already this drift would cause a distortion of the peak intensities in the deposition process. This is a plausible systematic error, which could be caused by instabilities in the deposition process. Thus is a distortion occurring through a drift in the deposition process. We shall calculate the distortion of periodicity and further strengthen that argument, ill-defined model which could not be reconstructed. To thus lead to a more complex, ill-defined model which could not be reconstructed. To would assume a more complex situation than the simple assumption of periodicity and compensate by tuning the parameters of the gradiant interface model, this assumption compensates a drift by tuning the parameters of the gradiant interface model, this assumption leads to effects the case. Although situations may occur, where the aperiodicities could lead to effects peaks symmetry, most prominently in the EUV curve, would be observed, which is not aperiodicities. In that case, however, a broadening of the peak or a distortion of the above. Those include drifts of the period thickness D across the stack or other systematic drifts, which are not covered by a strictly periodic model as the one introduced be imagined, which are not covered by a strictly periodic model as the one introduced at that point, it should be noted that other distortions of a perfect layer system can deliver information on the spatial distribution of the materials within one period.

At that point, it should be noted that other distortions of a perfect layer system can be excluded with certainty through the comparison shown in Fig. 4.21. The main difference of both models is the local gradiant change of the index of refraction, which may intermix differently with respect to the specific interface, i.e. the situation where attributes for the fact that both materials may intermix. More importantly, both materials are limited case of the binary model, which is still possible for the new gradiant model, provided through the appearance of a second Bragg peak in the XRR curve. Therefore, adding complementary information. In case of the example above, that information is same time, the results show that a verification of the model only becomes possible by than the binary approach by offering a reconstruction satisfying both data sets. At the

recorded within the interval from $\alpha_i = 2.5^\circ$ to $\alpha_i = 19.0^\circ$, with varying upper and lower

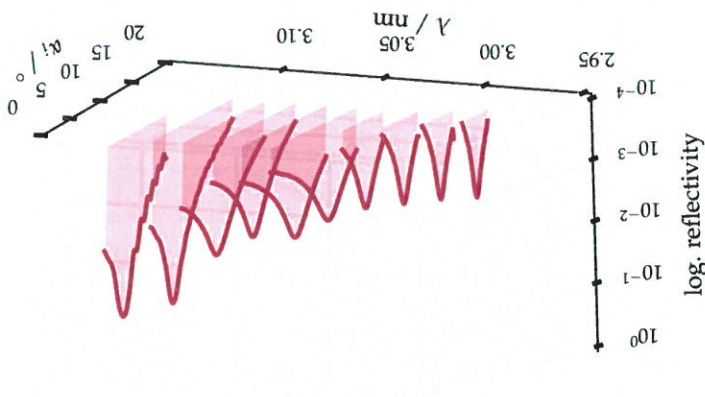


Figure 4.23 | Measured resonant EUV reflectivity curves across the Sc L2 and L3 edge in logarithmic representation. At each equidistant photon energy point, an angular resolution was resolved reflecting across the Bragg peak. [S]

The corresponding measurements are shown in Fig. 4.23. Each reflectivity curve was range, any change of contrast and absorption can be attributed to the Sc in the multilayer. As the Cr dispersion is changing only marginally and smoothly across the multilayer, across the first Bragg peak were recorded at several wavelengths that wavelength curves information contained in the optical constants of Sc, angular resolved reflectivity curves with the respective optical constants of Cr in Fig. 3.11 of Sec. 3.4.1 in Ch. 3. To exploit the L3 and L2 absorption edges at approximately $\lambda_{Sc-L} \approx 3.1$ nm and below by Aquila et al. [5]. The real and imaginary parts obtained from that experiments are shown together from that kind of experiment. In case of Sc, those were measured precisely for the Sc optical constants are necessary reducing quantitative information reflectivity experiments in the EUV spectral range promising. The knowledge of the total amount of Sc and equivalently Cr within a single period. For that purpose, resonant discussed here with possibly strong interdiffusion, a technique is required that yields the concerning the small total layer thickness in the Cr/Sc systems. For the particular system in Sec. 4.2.2 did improve the result but still shows fairly large confidence intervals analyzing the EUV curve. Similarly, the combined analysis of EUV and XRR experiments individual layer thicknesses in the range below 1 nm could not be obtained by exclusively seen for the four layer system discussed in Sec. 4.1, confidence intervals for the

Resonant EUV Reflectivity

Due to the increased complexity of the model, the question arises how accurately any parameter of the model can be determined and whether correlations exist and can be resolved (cf. Fig. 4.11 as an example for correlated model parameters in case of Mo/Si multilayer systems) based on the available data and whether further analytical measurements can improve the result as this was clearly the result for the combination of EUV and XRR experiments shown above. For the particular case of the gradual interface model for periodic multilayer systems with sub-nanometer thicknesses, in total four experiments were conducted to study the applicability of each method with respect to finding a unequivocal reconstruction including confidence intervals. Only by reconstructing the model resembling the reality inside the sample becomes possible, systematically analyzing the strength and weaknesses of the employed analytic methods, a reconstruction of the model reconstructing the strengths and weaknesses of the employed analytic methods. Only by

4.3.3 Addition of Complementary Experimental Methods

The sample was measured exciting fluorescence of the Sc and Cr K-lines, which show the highest fluorescence yield for the core shell transitions. The K-edges for both materials are at energies of $E_{Sc-K} = 4492\text{ eV}$ and $E_{Cr-K} = 5989\text{ eV}$ [5]. The experiment was therefore conducted at the four crystal monochromator (FCM) beamline at BESSY II and $\alpha_i \approx 3.62^\circ$, respectively. The Bragg peak is found at grazing angles of incidence of $\alpha_i \approx 4.12^\circ$ and $\alpha_f \approx 3.62^\circ$, respectively. The measured relative fluorescence yield in the vicinity of energy was used, the Bragg peak is shown in Fig. 4.24 for both photon energies and materials. Here, the first Bragg peak is shown in Fig. 4.24 for both photon energies and materials. Here, the K-edge of Cr, only data for the Sc K-fluorescence exists. In the second case, fluorescence X-ray fluorescence (GIXRF). Since the photon energy of $E_{ph} = 5500\text{ eV}$ is below the K-edge of Cr, the scattering angle of incidence, the method is referred to as grazing incidence due to the grazing angles of incidence. The method is referred to as grazing incidence due to the grazing angles of incidence. The grazing angle of incidence of $\alpha_i \approx 4.12^\circ$ was used, the Bragg peak is found at grazing angles of incidence of $\alpha_i \approx 4.12^\circ$, well above the respective edges as described in Ch. 3, Sec. 3.3. Depending on which in grazing incidence geometry at photon energies of $E_{ph} = 5500\text{ eV}$ and $E_{ph} = 6250\text{ eV}$, was therefore conducted at the four crystal monochromator (FCM) beamline at BESSY II was the grazing incidence geometry at photon energies of $E_{ph} = 6250\text{ eV}$. The details of the method and how spectral sensitivity can be obtained are described in detail in Ch. 2, Sec. 2.5.

The details of the method and how spectral sensitivity can be obtained are described in detail in Ch. 2, Sec. 2.5. The details of the method and how spectral sensitivity can be obtained are described in detail in Ch. 2, Sec. 2.5.

The sample was measured exciting fluorescence of the Sc and Cr K-lines, which show the highest fluorescence yield for the core shell transitions. The K-edges for both materials are at energies of $E_{Sc-K} = 4492\text{ eV}$ and $E_{Cr-K} = 5989\text{ eV}$ [5]. The experiment was therefore conducted at the four crystal monochromator (FCM) beamline at BESSY II and $\alpha_i \approx 3.62^\circ$, respectively. The Bragg peak is found at grazing angles of incidence of $\alpha_i \approx 4.12^\circ$ and $\alpha_f \approx 3.62^\circ$, respectively. The measured relative fluorescence yield in the vicinity of energy was used, the Bragg peak is shown in Fig. 4.24 for both photon energies and materials. Here, the first Bragg peak is shown in Fig. 4.24 for both photon energies and materials. Here, the K-edge of Cr, only data for the Sc K-fluorescence exists. In the second case, fluorescence X-ray fluorescence (GIXRF). Since the photon energy of $E_{ph} = 5500\text{ eV}$ is below the K-edge of Cr, the scattering angle of incidence, the method is referred to as grazing incidence due to the grazing angles of incidence. The method is referred to as grazing incidence due to the grazing angles of incidence. The grazing angle of incidence of $\alpha_i \approx 4.12^\circ$ was used, the Bragg peak is found at grazing angles of incidence of $\alpha_i \approx 4.12^\circ$, well above the respective edges as described in Ch. 3, Sec. 3.3. Depending on which in grazing incidence geometry at photon energies of $E_{ph} = 5500\text{ eV}$ and $E_{ph} = 6250\text{ eV}$, was therefore conducted at the four crystal monochromator (FCM) beamline at BESSY II was the grazing incidence geometry at photon energies of $E_{ph} = 6250\text{ eV}$. The details of the method and how spectral sensitivity can be obtained are described in detail in Ch. 2, Sec. 2.5.

In addition to the reconstruction of the Sc content via the REUV experiment, spectral resolved measurements are necessary to deduct the interface profile in the gradual layer

Grazing Incidence X-ray Fluorescence

shown below in this section.

UV experiment in Sec. 4.3.1. The details of the reconstruction based on this dataset are taken into account for the multilayer inhomogeneity deduced as described for the layer model and the optical constants by Aquila et al. [5]. The experimental uncertainties were estimated on basis of the resonant extreme ultraviolet reflectivity (REUV) experiment in Sec. 4.3.2, asymmetric interface regions provide a possibility to model. As discussed in Sec. 4.3.2, asymmetric interface regions provide a possibility to observe a second Bragg peak in the XRR measurement, even though both layers in the period have equal nominal thickness. To obtain information on that spectral distribution of both materials within a period, X-ray fluorescence (XRF) experiments exploiting the formation of a standing wave when scanning across the first Bragg peak were performed. The details of the method and how spectral sensitivity can be obtained are described in detail in Ch. 2, Sec. 2.5.

The results are compiled in Table 4.11. The confidence intervals were calculated by evaluating the probability distribution as a result of the MCMC procedure for each parameter. The confidence intervals given here represent percentiles of the number of samples found in the interval defined by the upper and lower bounds used for the PSO procedure for each parameter. In the case of a centred Gaussian distribution, percentiles of 2.3% and 97.8% of the integrated number of samples forming the distribution, mark the interval of four times the standard deviation, i.e. $\pm 2\sigma$ in statistical terms. Due to potential asymmetries in the actual distributions found by the MCMC method, explicit upper and lower bounds of the confidence intervals are given in table 4.11 based on these percentiles. The best model value is calculated by the MCMC sampling by taking the 50% percentile, of the distribution of the numerical parameter samples.

Before discussing the achieved reconstruction and the corresponding confidence intervals of each of the methods in detail, we shall view the theoretical curves calculated from the best model of the combined analysis. The curves are shown in direct comparison with the data from Fig. 4.25 including the respective experimental uncertainties in Fig. 4.26. Clearly, the data and the solution found in the optimization procedure show excellent agreement indicating that the dual interface model indeed provides a very good representation of the multilayer structure with respect to the experiments conducted here. Nevertheless, differences can be observed. The reason lies in the fact that the model is potentially still rather ideal. Small variations during the deposition process, for example, could lead to imperfections, which are not described in a strictly periodic model. How-

As discussed numerously throughout this chapter, the PSO ideally delivers the global minimum of the respective optimization functional. However, no information is obtained about the uniqueness and accuracy of the solution or correlation of parameters causing ambiguity of the results. Consequently, in addition to fitting the data with a particle swarm optimizer, the result was verified based on the MCMC method described above to evaluate the confidence intervals for each parameter. To assess the performance of each of the experimental methods individually, the two step process, i.e. the PSO fitting procedure followed by the MCMC sampling, was conducted for each stand-alone experiment as well as for the combined optimization problem stated in Eq. (4.9).

Loquidene Intervals and Evaluation of the Experimental Methods

↳ school will direct audience: a select society

Parameter	D / nm	T_{Sc}	s_d / nm	T_o	η	a_r / nm	P_{Sc}	P_{Sc}	P_{Cr}
Combined	1.5737 ± 0.0008	1.5749 ± 0.0014	1.5726 ± 0.0035	1.5728 ± 0.0016	1.5741 ± 0.0021	0.48 ± 0.04	0.35 ± 0.14	0.42 ± 0.35	0.49 ± 0.09
EUV	1.5737 ± 0.0008	1.5749 ± 0.0014	1.5726 ± 0.0035	1.5728 ± 0.0016	1.5741 ± 0.0021	0.48 ± 0.04	0.35 ± 0.14	0.42 ± 0.35	0.49 ± 0.09
XRR	1.5737 ± 0.0008	1.5749 ± 0.0014	1.5726 ± 0.0035	1.5728 ± 0.0016	1.5741 ± 0.0021	0.48 ± 0.04	0.35 ± 0.14	0.42 ± 0.35	0.49 ± 0.09
REUV	1.5737 ± 0.0008	1.5749 ± 0.0014	1.5726 ± 0.0035	1.5728 ± 0.0016	1.5741 ± 0.0021	0.48 ± 0.04	0.35 ± 0.14	0.42 ± 0.35	0.49 ± 0.09
GIXRF	1.5737 ± 0.0008	1.5749 ± 0.0014	1.5726 ± 0.0035	1.5728 ± 0.0016	1.5741 ± 0.0021	0.48 ± 0.04	0.35 ± 0.14	0.42 ± 0.35	0.49 ± 0.09

Table 4-11 Optimized model parameters with confidence intervals derived from MCMC validation for each individual experiment and the combined analysis

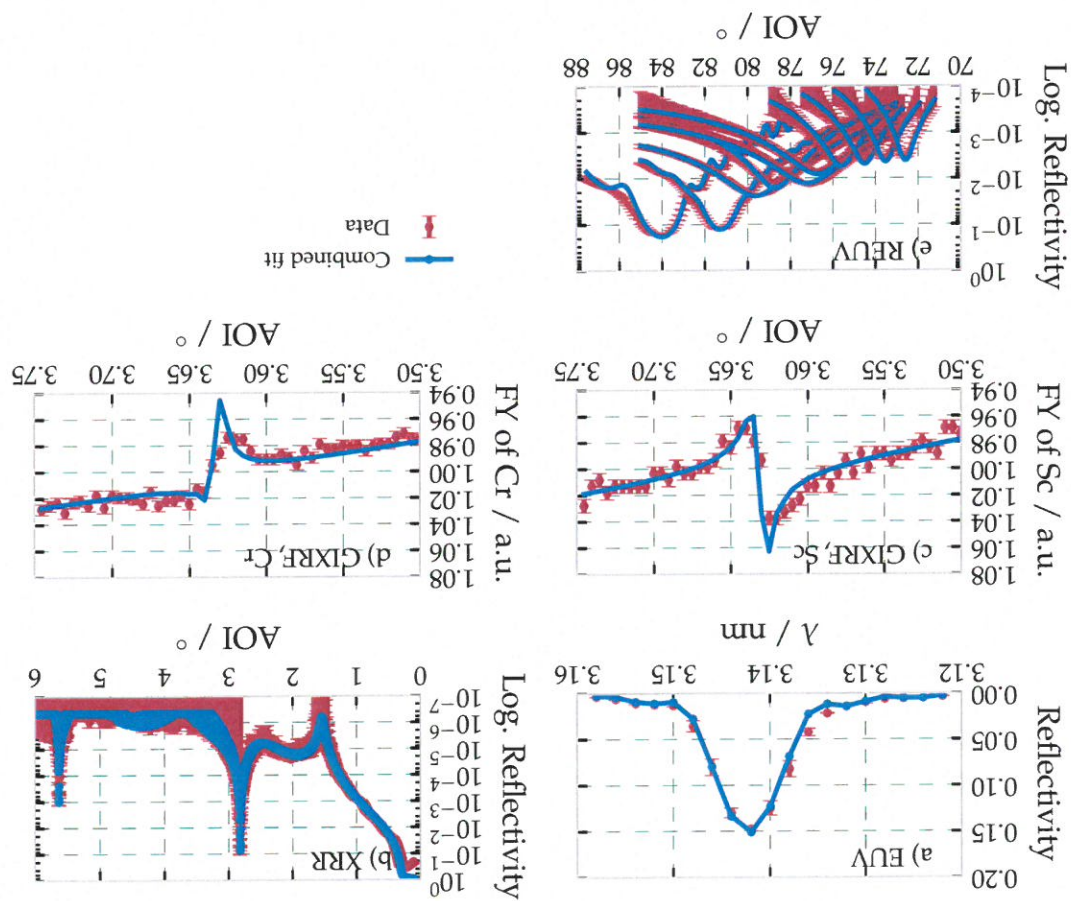


Figure 4.26 | Measured reflectance and fluorescence yield curves in direct comparison with the calculated reflectance and intensity curves for the optimized parameters obtained through the combined analysis of all experiments as listed in table 4.11.

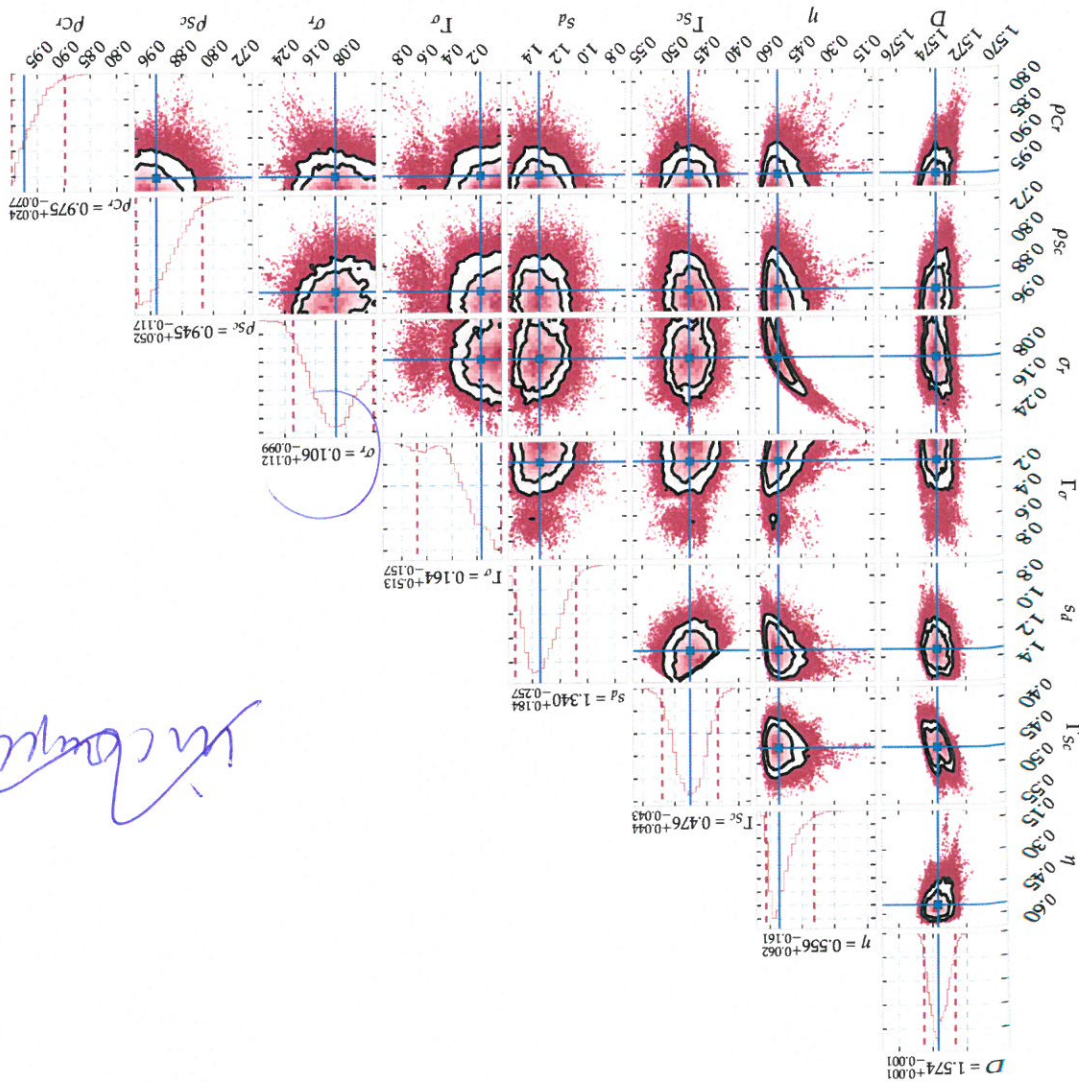
Finally, the parameter set of the r.m.s. roughness σ , and the interdiffusion parameter η dimensions and frequencies expected in the order of nanometres. Thereby, any reflected covering and area of approximately 1 mm by 1 mm, in comparison to the roughness shall consider the relatively large beam footprint, with the smallest one of all experiments separate the effect of roughness and interdiffusion. For better understanding this, we conclusion can easily be understood as none of the applied experimental methods can consequently physical properties of the sample, based on the analyzed data. In fact, this in both parameters hints at a indistinguishability of those two model parameters, and better illustrate this property. The broad spectrum of values covered by the distribution for both parameters. Fig. 4.28 shows a magnification of that particular histogram to show a "banana shaped" correlation significantly broadening the confidence intervals and the parameter set of the r.m.s. roughness σ , and the interdiffusion parameter η actual structure present in the sample.

minimizing the χ^2 functional and it may thus be concluded that this corresponds to the analysis as it clearly demonstrates that only strongly asymmetric interface regions are emphasized on the lower value. That is a particularly interesting result of the combined parameter shows a bimodal distribution for all two-dimensional histograms with clear densities p_{Sc} and p_{Cr} , as well as for the interface region ratio T . In addition, the latter mathematical restrictions on the parameters as discussed in Sec. 4.3.2, such as for the cases, the distribution is truncated by parameter limits, which follow from physical or for a unique solution with corresponding uncertainty. It should be noted that in some approach the shape of a two-dimensional Gaussian distribution, which would be expected generally, most of the parameter combinations do not show distinct correlations but optimized model as listed in table 4.11 for the combined analysis column.

Parameter correlations in the combined analysis

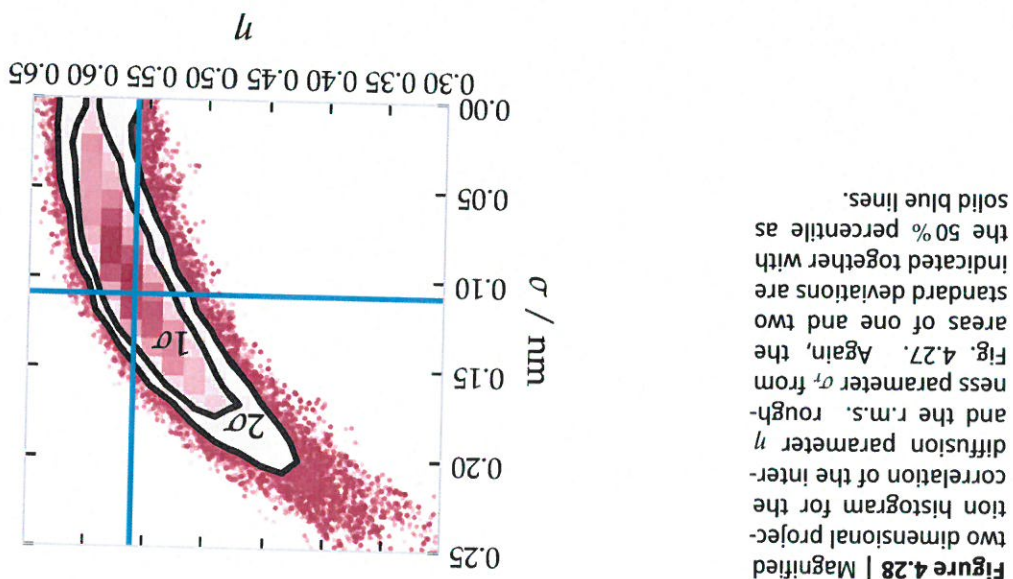
With the optimized model parameters listed in table 4.11 and shown in Fig. 4.26 for the combined analysis, a model reconstruction could be obtained explaining the data from the individual measurements by measuring the EUV reflectivity at positions ± 2 mm of the different experimental setups. The latter effects were considered in the uncertainties the sample, which causes mismatches in the measurement position varies slightly between the deviation in the homogeneity of the sample, e.g. a varying period across the model with a vastly increased number of parameters and is thus not practical. Another reason is the deviation in the periodicity of the sample, e.g. a varying period across the sample over 4 mm across the sample.

Figure 4.27 | Matrix representation of the result of the maximum likelihood analysis based on the MCMC method for all parameter combinations. At the top of each column, the one-dimensional projection of the likelihood distribution for the respective parameter is shown in analogy to the figures for a discussion of the observed features see main text. The solid black contours mark the areas for one and two standard deviations, respectively. The dotted red lines indicate the $\pm 2\sigma$ interval, i.e. two standard deviations from the center value (50 % percentile). The latter is indicated through the solid blue lines. In the two dimensional projections, the solid blue contours mark the areas for one and two standard deviations, respectively.



Confidence intervals depending on the employed method

radiation or fluorescence excitation within the multilayer always represents an average of the rough interface morphology. That, however, can not be distinguished from a homogeneous layer with radial interdiffusion along the surface normal of the sample. The solution to this problem of distinction is the analysis of diffuse scattering from the sample in addition to the combined analysis, which is the topic of the Ch. 5 of this thesis.



CHARACTERIZATION OF THE MULTILAYER STRUCTURE FOR DIFFERENT SYSTEMS

en. In: *Journal of Applied Crystallography* 49, 6 (Dec. 2016), pp. 2161–2171. doi: 10.1107/[S1600576716015776](https://doi.org/10.1107/S1600576716015776)

The experiments, methods and findings of this section are part of the publication A. Haase, S. Bajt, P. Hönigk, V. Soltwisch and F. Scholze, *Multiparameter characterization of subnanometer Cr/Sc multilayers based on complementary measurements*, *Chapter 5*.

be verified by the aforementioned analysis of diffuse scattering. This is the topic of that due to the correlation between roughness and interdiffusion this result is still to respect to the binary model, causes the diminished reflectivity. We should note, however, maximum, this shows that intermixing is the main reason. The loss of contrast with stack pure Sc or pure Cr layers are observed, but always a mixture of both. In the context of answering the question of poor reflectivity with respect to the theoretical possibility of a remarkable result of the combined analysis is the strong asymmetry of the interdiffusion layers. This can only be shown by the combination of all analytical experiments conducted here. In addition, the comparison shows that at no point within the periodic multilayer in direct comparison with the initial binary model. As mentioned before, the most thicknesses is shown in Fig. 4.30 by the depth dependence of the index of refraction. The final result of this analysis of Cr/Sc multilayer systems with sub-nanometer layer broadest by the analysis conducted here.

case of Cr/Sc multilayers, the Cr is heavier and thus has higher momentum leading to a broader interdiffusion layer, which is indeed also the interface region found to be the in thicker interdiffusion layer, which is indeed also the interface region found to be the

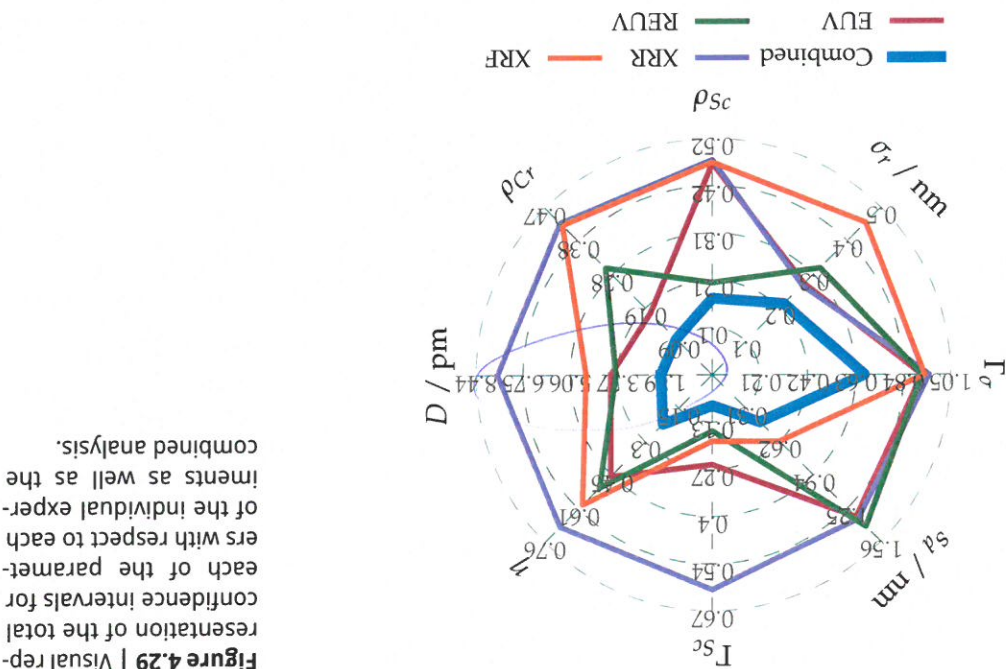


Figure 4.29 | Visual representation of the total confidence intervals for each parameter of the individual experiments with respect to each other. Each of the parameters is represented by a color-coded line. The combined analysis is represented by a green line. The individual experiments are represented by red, blue, and orange lines. The combined analysis is the broadest, followed by the individual experiments as well as the combined analysis.

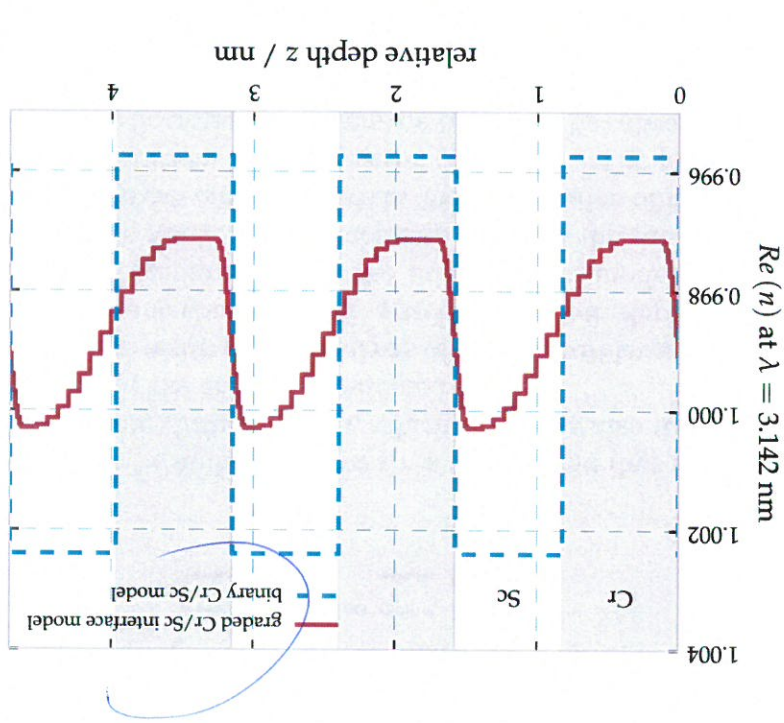


Figure 4.30 | Real part of the index of refraction based on the results of the optimised parameters listed in Table ?? for the combined analysis for a selected wavelength. The gradual interface model is shown in detail comparing to the binary model optimised for the EUV reflectance curve over three full periods. The resulting strong asymmetry in the width of the interference fringes is clearly visible (see text). The gray and white shaded areas indicate the Cr and Sc layers respectively, for the binary model.

- [1] M. Abramowitz and I. A. Stegun: *Handbook of Mathematical Functions: With Formulas, Graphs, and Mathematical Tables*. en. Courier Corporation, 1964.
- [2] J. Als-Nielsen and D. McMorrow: *X-rays and their interaction with matter*, en.
- [3] C. Amra: 'From light scattering to the microstructure of thin-film multilayers', In: *Appl. Opt. 32.28 (1993)*, pp. 5481–5491, doi: 10.1364/AO.32.005481.
- [4] C. Amra: 'Light scattering from multilayer optics. I. Tools of investigation', In: *J. Opt. Soc. Am. A 11.1 (1994)*, pp. 197–210, doi: 10.1364/JOSAA.11.000197.
- [5] A. L. Aquila, F. Salmassi, E. M. Gullikson, F. Eriksson and J. Birch: 'Measurements of the optical constants of scandium in the 50–1300eV range', In: *vol. 5538. 2004, pp. 64–71*, doi: 10.1117/12.563615.
- [6] S. Bajt, J. B. Alameda, T. W. Barbee Jr., W. M. Cliff, J. A. Folta, B. Kaufman and E. A. Spiller: 'Improved reflectance and stability of Mo-Si multilayers', In: *Optical Engineering 41.8 (2002)*, pp. 1797–1804, doi: 10.1117/1.1489426.
- [7] S. Bajt, D. G. Stearns and P. A. Kearney: 'Investigation of the amorphous-to-crystalline transition in Mo/Si multilayers', In: *Journal of Applied Physics 90.2 (2001)*, pp. 1017–1025, doi: <http://dx.doi.org/10.1063/1.1381559>.
- [8] A. Ballerma and S. Mobilio: 'Introduction to Synchrotron Radiation', en. In: *Synchrotron Radiation*. Ed. by S. Mobilio, F. Boscherini and C. Meneghini, DOI: 10.1007/978-3-642-55315-8_1. Springer Berlin Heidelberg, 2015, pp. 3–28.
- [9] J. Barbee Troy W., J. W. Weed, R. B. Hoover, M. J. Allen, J. F. Lindblom, R. H. O’Neal, C. C. Kankeleborg, C. E. DeForest, E. S. Paris, A. B. C. Walker II, T. D. Willis, E. S. Gluskin, P. A. Pianetta and P. C. Bakker: 'Multi-Spectral Solar Telescope Array III: soft x-ray EUV reflectivity of the multilayer mirrors', In: *Optical Engineering 30.8 (1991)*, pp. 1067–1075, doi: 10.1117/12.55917.
- [10] T. W. Barbee, S. Mrowka and M. C. Hettick: 'Molybdenum-silicon multilayer mirrors for the extreme ultraviolet', In: *Appl. Opt. 24.6 (1985)*, pp. 883–886, doi: 10.1364/AO.24.000883.
- [11] M. Bayes and M. Price: 'An Essay towards Solving a Problem in the Doctrine of Chances. By the Late Rev. Mr. Bayes', F. R. S., en. In: *Philosophical Transactions 53 (1763)*, Letter to John Canton, A. M. F. R. S., en. In: *Philosophical Transactions 53 (1763)*.

References

- [12] B. Beckhoff, A. Gotwald, R. Klein, M. Krumrey, R. Müller, M. Richter, F. Scholze, R. Thomm, G. Ullm, A. J. Leenarts and W. W. Hogenholt: "The Influence of X-ray Fluorescence on the Reflectivity and Angle-Dependent X-ray Fluorescence", In: *Physica Status Solidi* (b) **246**, pp. 1415–1434, DOI: 10.1002/pssb.200945162.
- [13] F. d. Bergveld: "The Interaction of X-Rays (and Neutrons) with Matter", In: *X-ray and Neutron Reflectivity*, Ed. by J. Daillant and A. Gibaud, Lecture Notes in Physics **770**, DOI: 10.1007/978-3-540-88588-7_1, Springer Berlin Heidelberg, 2009, pp. 1–57.
- [14] R. T. Birge: "The Calculation of Errors by the Method of Least Squares", In: *Physical Review* **40**, pp. 207–227, DOI: 10.1103/PhysRev.40.207.
- [15] D. K. C. de Boer, A. J. G. Leenarts and W. W. Hogenholt: "Influence of Roughness Profile on Reflectivity and Angle-Dependent X-ray Fluorescence", In: *J. Phys. III France* **4**, pp. 1559–1564, DOI: 10.1051/jph:1994222.
- [16] D. K. C. de Boer: "Glaucous-Incidence X-ray Fluorescence of Layered Materials", In: *Physical Review B* **44**, pp. 498–511, DOI: 10.1103/PhysRevB.44.498.
- [17] D. K. C. de Boer: "X-ray Reflection and Transmission by Rough Surfaces", In: *Phys. Rev. B* **51**, pp. 5297–5305, DOI: 10.1103/PhysRevB.51.5297.
- [18] D. K. C. de Boer: "X-ray Scattering and X-ray Fluorescence from Materials with Rough Interfaces", In: *Phys. Rev. B* **53**, pp. 6048–6064, DOI: 10.1103/PhysRevB.53.6048.
- [19] F. R. Boer: "Cohesion in metals: transition metal alloys", en. North-Holland, 1988.
- [20] R. Bonifacio, C. Pellegrini and L. M. Narducci: "Collective instabilities and high-gain regime in a free electron laser", In: *Optics Communications* **50**, pp. 373–378, DOI: 10.1016/0030-4018(84)90105-6.
- [21] M. Born and E. Wolf: *Principles of Optics*, 3rd ed., Cambridge University Press,
- [22] G. Brandt, J. Eden, R. Filegauf, A. Gotwald, A. Hoehl, R. Klein, R. Müller, M. Richter, F. Scholze, R. Thomm, G. Ullm, K. Birkmann, J. Rahm and G. Wuestefeld: "The Metrology Light Source – The new dedicated electron storage ring of PTB", In: *Nuclear Instruments and Methods in Physics Research Section B: Beam Interactions with Materials and Atoms* **258**, pp. 445–452, DOI: 10.1016/j.nimb.2007.02.076.
- [23] S. Braun, T. Foltyń, H. Mai, M. Moss and A. Leson: "Grenzfällchen-optimeter optimised Mo/Si multilayers as reflectors for the EUV spectral range", In: *Vak-Mo/Si Multischichten als Reffektoren für den EUV Spektralbereich. Interfacen mit unterschiedlichen Mo/Si multilayers* and A. Leson: "Mo/Si Multilayers with different Barrier Layers for Applications as Extreme Ultraviolet Mirrors", In: *Japanese Journal of Applied Physics* **41**, pp. 4074, DOI: 10.1143/JJAP.41.4074.
- [24] S. Braun, H. Mai, M. Moss, R. Scholze and A. Leson: "Mo/Si Multilayers with different Barrier Layers for Applications as Extremes Ultraviolet Mirrors", In: *Proceedings of The Workshop On particle Swarm Optimization*, Indianapolis, USA, 2001.
- [25] A. Carlisle and G. Dozier: "An off-the-shelf PSO", In: *Proceedings of The Workshop On particle Swarm Optimization*, Indianapolis, USA, 2001.
- [26] D. R. Cox and D. V. Hinkley: *Theoretical Statistics*, en. CRC Press, 1979.
- [27] J. W. Criss and L. S. Birks: "Calculation methods for fluorescence x-ray spectrometry", In: *Analytical Chemistry* **40**, pp. 1080–1086, DOI: 10.1021/ac60263a023.

- [28] Croce, P. and Nevot, L.: *Étude des couches minces et des surfaces par réflexion rasante, spéciale de diffuse, de rayons X*. In: *Riv. Phys. Appl. (Paris)* **11**, pp. 113–125. DOI: 10.1051/rphysap:01976001101011300.
- [29] J. Daillant, S. Mora and A. Senechal: *Diffuse Scattering*, en. In: *X-ray and Neutron Reflectivity*. Ed. by J. Daillant and A. Gibaud. Lecture Notes in Physics 770. DOI: 10.1007/978-3-540-88588-7_4. Springer Berlin Heidelberg, 2009, pp. 133–182.
- [30] J. Daillant, A. Gibaud, W. Beiglböck, J. Ehlers, K. Hepp, H. A. Schwetman and R. Heidelberger, 2009.
- [31] D. A. G. Deacon, L. R. Elias, J. M. J. Maday, G. J. Ramian, H. A. Schwetman and T. I. Smith: *First Operation of a Free-Electron Laser*. In: *Physical Review Letters* **38**, 16 (1977), pp. 892–894. DOI: 10.1103/PhysRevLett.38.892.
- [32] Y. S. Derbenev, A. M. Kondratenko and E. L. Saldin: *On the Possibility of Using a Free Electron Laser for Polarization of Electrons in Storage Rings*. In: *Nuclear Instruments and Methods in Physics Research* **193**, 3 (1982), pp. 415–421. DOI: 10.1016/0029-554X(82)90233-6.
- [33] B. N. Dev, A. K. Das, S. Dev, D. W. Schubert, M. Stamm and G. Materlik: *Resonance enhancement of x rays in layered materials: Application to surface enrichment*. In: *Proceedings of the Cambridge Philosophical Society* **35**, 3 (1939), pp. 416–418. DOI: 10.1017/S0305004100021162.
- [34] P. a. M. Dirac: *A new notation for quantum mechanics*. In: *Mathematical Proceedings of the Cambridge Philosophical Society* **35**, 3 (1939), pp. 121–128. DOI: 10.1016/S0969-806X(01)00227-4.
- [35] W. T. Elam, B. D. Ravel and J. R. Sieber: *A new atomic database for X-ray spectroscopic calculations*. In: *Radiation Physics and Chemistry* **63**, 2 (2002), pp. 121–128. DOI: 10.1016/S0969-806X(01)00227-4.
- [36] J. M. Elson, J. P. Rahm and J. M. Bennet: *Light scattering from multilayer optics: Comparison of theory and experiment*. In: *Appl. Opt.* **19**, 5 (1980), pp. 669–679. DOI: 10.1364/AO.19.000669.
- [37] J. M. Elson, J. P. Rahm and J. M. Bennet: *Relationship of the total integrated reflectivity of Cr/Sc multilayers by ion-assisted sputter deposition*. In: *Optical Engineering* **41**, 11 (2002), pp. 2903–2909. DOI: 10.1117/1.1510750.
- [38] F. Eriksson, G. A. Johansson, H. M. Hertz, E. M. Gulliksson, U. Kreissig and J. Birch: *Enhanced soft x-ray reflectivity of Cr/Sc multilayers by ion-assisted sputter deposition*. In: *Optical Engineering* **41**, 11 (2002), pp. 2903–2909. DOI: 10.1117/1.1510750.
- [39] F. Eriksson, G. A. Johansson, H. M. Hertz, E. M. Gulliksson, U. Kreissig and J. Birch: *14.5% near-normal incidence reflectance of Cr/Sc x-ray multilayer mirrors for the water window*. In: *Opt. Lett.* **28**, 24 (2003), pp. 2494–2496. DOI: 10.1364/OL.28.24.002494.

- [40] T. Feigl, S. Yulin, N. Benoit and N. Kaiser: '(EUV) multilayer optics'. In: *Micro-electronic Engineering* 83.4-9 (2006). Micro- and Nano-Engineering [MNE] 2005 Proceedings of the 31st International Conference on Micro- and Nano-Engineering [MNE] 2005 pp. 703-706. doi: <http://dx.doi.org/10.1016/j.mee.2005.12.033>.
- [41] M. Finkenhahl, A. P. Zwicker, S. P. Regan, H. W. Moos and D. Stutman: 'Near normal incidence spectroscopy of a Penning ionization discharge in the 110-180 Å range with flat multilayer mirrors'. In: *Applied Optics* 29.24 (1990), p. 3467. doi: 10.1364/AO.29.003467.
- [42] D. Foreman-Mackey, D. W. Hogg, D. Lang and J. Goodman: 'emcee: The MCMC Hammer'. In: *Publications of the Astronomical Society of the Pacific* 125.925 (2013). arXiv: 1202.3665, pp. 306-312. doi: 10.1086/670067.
- [43] C. F. Gauss: 'Theoria motus corporum coelestium in sectionibus conicis sollem ambientium. en. 1809.
- [44] N. Ghafour, F. Eriksson, E. Gullikson, L. Hultman and J. Birch: 'Incorporation of nitrogen in Cr/Sc multilayers giving improved soft x-ray reflectivity'. In: *Applied Physics Letters* (2008). doi: 10.1063/1.2857459.
- [45] S. K. Ghose and B. N. Dev: 'X-ray standing wave and reflectometric characterization of multilayer structures'. In: *Physical Review B* 63.24 (2001), p. 245409. doi: 10.1103/PhysRevB.63.245409.
- [46] A. Gibaud and G. Vignaud: 'Specular Reflectivity from Smooth and Rough Surfaces'. In: *X-ray and Neutron Reflectivity*. Ed. by J. Daillant and A. Gibaud. Lecture Notes in Physics 770. DOI: 10.1007/978-3-540-88588-7_3. Springer Berlin Heidelberg, 2009, pp. 85-131.
- [47] J. Goodman and J. Weare: 'Ensemble samples with affine invariance'. In: *Communications in Applied Mathematics and Computational Science* 5.1 (2010), pp. 65-80. doi: 10.2140/camcos.2010.5.65.
- [48] E. M. Gullikson and D. G. Stearns: 'Asymmetric extreme ultraviolet scattering from sputter-deposited multilayers'. In: *Phys. Rev. B* 59.20 (1999), pp. 13273-13277. doi: 10.1103/PhysRevB.59.13273.
- [49] A. Haase, S. Baft, P. Honnike, V. Solwitsch and F. Scholze: 'Multiparameter characterization of subnanometre Cr/Sc multilayers based on complementary measurements'. In: *Journal of Applied Crystallography* 49.6 (2016), pp. 2161-2171. doi: 10.1107/S1600576716015776.
- [50] A. Haase, V. Solwitsch, S. Braun, C. Laubs and F. Scholze: 'Interfacial Morphology of Mo/Si Multilayer Systems with Varying Mo Layer Thickness Studied by EUV Diffuse Scattering'. In: *Optics Express* (2017).
- [51] A. Haase, V. Solwitsch, F. Scholze and S. Braun: 'Role of dynamic effects in the characterization of multilayers by means of power spectral density'. In: *Appl. Opt.* 53.14 (2014), pp. 3019-3027. doi: 10.1364/AO.53.003019.
- [52] A. Haase, V. Solwitsch, F. Scholze and S. Braun: 'Characterization of Mo/Si mirror scattering'. In: *Proc. SPIE*. Vol. 9628. 2015, pages. doi: 10.1117/12.2191265.

- [53] B. L. Henke, E. M. Gullikson and J. C. Davis; *X-Ray Interactions: Photoabsorption, Scattering, Transmission, and Reflection at $E = 50\text{-}30,000 \text{ eV}$* ; In: *Atomic Data and Nuclear Data Tables* **54**.2 (1993), pp. 181–342. doi: <http://dx.doi.org/10.1006/adnd.1993.1013>.
- [54] H. M. Hertz, L. Rytlew, M. Berglund, G. A. Johansson, T. Willheim, Y. Y. Platonov and D. M. Broadaway; *Normal-incidence condenser mirror arrangement for compact water-window x-ray microscopy*. In: *Proc. SPIE* **3766** (1999), pp. 247–251. doi: 10.1117/12.363641.
- [55] M. P. Hobson and J. E. Baldwin; *Markov-chain Monte Carlo approach to the design of multilayer thin-film optical coatings*. EN. In: *Applied Optics* **43**.13 (2004), pp. 2651–2660. doi: 10.1364/AO.43.002651.
- [56] V. Holý and T. Baumback; *Nonspecular X-ray reflection from rough multilayers*. In: *Phys. Rev. B* **49**.15 (1994), pp. 10668–10676. doi: 10.1103/PhysRevB.49.10668.
- [57] V. Holý, J. Kubena, I. Ohndal, K. Lischka and W. Plotz; *X-ray reflection from diffuse scattering from multilayers with rough interfaces*. In: *Phys. Rev. B* **52**.23 (1995), pp. 16369–16372. doi: 10.1103/PhysRevB.52.16369.
- [58] V. M. Kaganer, S. A. Stepanov and R. Kohlér; *Bragg diffraction peaks in x-ray (1995)*, pp. 16369–16372. doi: 10.1103/PhysRevB.52.16369.
- [59] J. Kennedy; *Particle Swarm Optimization*, en. In: *Encyclopediad of Machine Learning*. Ed. by C. Sammut and G. I. Webb. DOI: [10.1007/978-0-387-30164-8_630](https://doi.org/10.1007/978-0-387-30164-8_630). Springer US, 2011, pp. 760–766.
- [60] H. Kiessig; *Interferenz von Röntgenstrahlen an dünnen Schichten*. In: *Annalen der Physik* **402**.7 (1931), pp. 769–788. doi: 10.1002/andp.19314020702.
- [61] J. Kitz, C. Jacobsen and M. Howells; *Soft X-ray microscopes and their biological applications*. In: *Quarterly Reviews of Biophysics* **28**.01 (1995), pp. 33–130. doi: 10.1017/S0033583500003139.
- [62] M. Krumrey; *Design of a Four-Crystal Monochromator Beamline for Radiometry at BESSY II*, en. In: *Journal of Synchrotron Radiation* **5**.1 (1998), pp. 6–9. doi: 10.1107/S0909049597011825.
- [63] L. D. Landau and E. M. Lifshitz; *Electrodynamics of Continuous Media*. A Course of Theoretical Physics 8. Oxford, London, New York, Paris: Pergamon Press, 1960.
- [64] H. Legeall, G. Blodel, H. Stiel, W. Sandner, C. Seim, P. Takman, D. H. Martz, M. Wirtz and W. Dietze; *Compact x-ray microscope for the water window based on a high brightness laser plasma source*. In: *Opt. Express* **20**.16 (2012), pp. 18362–18369. doi: 10.1364/OE.20.018362.
- [65] A.-M. Legendre; *Nouvelles méthodes pour la détermination des orbites des comètes*. fr. F. Didot, 1805.
- [66] K. Levenberg; *A method for the solution of certain non-linear problems in least squares*. In: *Quarterly of Applied Mathematics* (1944).
- [67] J. R. Levine, J. B. Cohen, Y. W. Chung and P. Georgeopoulos; *Grazing-incidence small-angle X-ray scattering: new tool for studying thin film growth*. In: *Journal of Applied Crystallography* **22**.6 (1989), pp. 528–532. doi: 10.1107/S00218898900717X.

- [68] Y. Lim, T. Westerwallebelsch, A. Aschenbrück, O. Wehmeyer, G. Haindl, U. Kleinert, U. Heimann: Fabractation and characterization of EUV multilayer mirrors optimized for small spectral reflection bandwidth. In: *Applied Physics A* 72.1 (2001), pp. 121–124. doi: 10.1007/s003390000723.
- [69] H. A. Lorenz: The theorem of Poynting concerning the energy in the electromagnetic field and two general propositions concerning the propagation of light. In: *Amsterdam Akademie der Wissenschaften* 4 (1896), p. 176.
- [70] J. Lübeck, B. Beckhoff, R. Fliegau, I. Höfleider, P. Honické, M. Müller, B. Polakowski, F. Reinhardt and J. Wesser: A novel instrument for quantitative nanoscale techniques involving complementary X-ray methodologies. In: *Review of Scientific Instruments* 84.4 (2003), p. 045106. doi: 10.1063/1.4798299.
- [71] D. J. Mackay: *Information Theory, Inference and Learning Algorithms*. en. Cambridge University Press, 2003.
- [72] J. M. J. Madey: Stimulated Emission of Bremsstrahlung in a Periodic Magnetic Structure. In: *Journal of Applied Physics* 42.5 (1971), pp. 1906–1913. doi: 10.1063/1.1660466.
- [73] D. W. Marquardt: An algorithm for least-squares estimation of nonlinear parameters. In: *Journal of the Society for Industrial and Applied Mathematics* 11.2 (1963), pp. 431–441.
- [74] D. S. Martinez-Galarce, I. Walker Arthur B., C., D., B., Gore, C., Kankeleborg, R. B. Hoover, J. Babcock T. W. and P. F. X. Borerer: High resolution imaging with optical engineering 39.4 (2000), pp. 1063–1079. doi: 10.1117/1.602468.
- [75] P. Mikulik: X-ray reflectivity from planar and structured multilayers. PhD thesis, These de l'Université Joseph Fourier, 1997.
- [76] J. S. Milton and J. C. Arnold: *Introduction to Probability and Statistics: Principles and Applications for Engineering and the Computing Sciences*. 4th. New York, NY, USA: McGraw-Hill, Inc., 2002.
- [77] S. V. Milton, E. Gluskin, N. D. Arnold, C. Benson, W. Berg, S. G. Biedron, M. Borland, Y.-C. Chae, R. J. Dejeus, P. K. D. Hartog et al.: Experimental Gain and Saturation of a Self-Amplified Spontaneous Emission Free-Electron Laser. In: *Science* 292.5524 (2001), pp. 2037–2041. doi: 10.1126/science.1059955.
- [78] I. H. Munro and G. V. Marr: CHAPTER 1 - SYNCHROTRON RADIATION SOURCES. In: *Handbook on Synchrotron Radiation*. Handbook on Synchrotron Radiation. Amsterdam: Elsevier, 1987, pp. 1–20.
- [79] H. Nakajima, H. Fujimoto and M. Kawai: Interdiffusion and structural relaxation in Mo/Si multilayer films. In: *Journal of Applied Physics* 63.4 (1988), pp. 1046–1051.
- [80] Nérot, L. and Croce, P.: Caractérisation des surfaces par réflexion rasante de rayons X. Application à l'étude du polissage de quilles verres silicates. In: *Réseaux Physiques* 15.3 (1980), pp. 761–779. doi: 10.1051/rphysap:0198001503076100.
- [81] A. K. Pettord-Long, M. B. Sterns, C.-H. Chang, S. R. Nutt, D. G. Sterns, N. M. Ceglio and A. M. Hawrylik: High-resolution electron microscopy study of x-ray multilayer structures. In: *Journal of Applied Physics* 61.4 (1987), pp. 1422–1428. doi: <http://dx.doi.org/10.1063/1.338122>.

- [82] U. Pietisch, V. Holz and T. Baumback: *High-Resolution X-Ray Scattering From Thin Films to Layered Nanostructures*. Springer, 2004.
- [83] M. Prascoli, A. Haase, F. Scholze, H. N. Chapman and S. Bajt: *Extended asymmetric-cut multilayer X-ray gratings*. EN. In: *Optics Express* 23.12 (2015), pp. 15195–15204. doi: 10.1364/OE.23.015195.
- [84] M. Prascoli, A. F. G. Leonowich, K. R. Beyrelein and S. Bajt: *Thermal stability studies of short period Sc/Cr and Sc/B4C/Cr multilayers*. In: *Appl. Opt.* 53.10 (2014), pp. 2126–2135. doi: 10.1364/AO.53.002126.
- [85] S. D. Rasberry and K. F. J. Heinrich: *Calibration for interelement effects in x-ray fluorescence analysis—theory*. In: *Analytical Chemistry* 46.1 (1974), pp. 81–89. doi: 10.1021/ac60337a027.
- [86] R. M. Rousseau: *Fundamental algorithm between concentration and intensity in XRF analysis I—theory*. en. In: *X-Ray Spectrometry* 13.3 (1984), pp. 115–120. doi: 10.1002/xrs.1300130306.
- [87] N. N. Salashchenko and E. A. Shamo: *Short-period X-ray multilayers based on Cr/Si*. In: *Optics Communications* 134.1–6 (1997), pp. 7–10. doi: [http://dx.doi.org/10.1016/S0030-4018\(96\)00551-2](http://dx.doi.org/10.1016/S0030-4018(96)00551-2).
- [88] T. Salldit, D. Lotz, T. H. Metzger, J. Peisl, G. Virginaud, P. Høghei, O. Schärf, F. Schäfers, H.-C. Mertins, F. Schmolla, I. Packe, N. N. Salashchenko and E. A. 2231. doi: 10.1103/PhysRevB.54.5860.
- [89] T. Salldit, T. H. Metzger and J. Peisl: *Kinetic Roughness of Amorphous Multilayers Studied by Diffuse X-Ray Scattering*. In: *Phys. Rev. Lett.* 73.16 (1994), pp. 2228–2231. doi: 10.1103/PhysRevB.54.5860.
- [90] F. Schäfers, H.-C. Mertins, F. Schmolla, I. Packe, N. N. Salashchenko and E. A. 2231. doi: 10.1103/PhysRevB.54.5860.
- [91] F. Scholze, J. Tümler and G. Ulm: *High-accuracy radiometry in the EUV range at the PTB soft x-ray beamline*. en. In: *Metrologia* 40.1 (2003), S224. doi: 10.1088/0026-1394/40/1/352.
- [92] F. Scholze, B. Beckhoff, G. Brandt, R. Fliegau, A. Gottwald, R. Klein, B. Meyer, U. D. Schwarz, R. Thormägel, J. Tümler, K. Vogel, J. Wesser and G. Ulm: *High-accuracy EUV metrology of PTB using synchrotron radiation*. In: *Proc. SPIE*. Vol. 4344. 2001, pp. 402–413. doi: 10.1117/12.436766.
- [93] S. Schröder, T. Heerfurth, H. Blaschke and A. Duپarre: *Angle-resolved scattering: an effective method for characterizing thin-film coatings*. In: *Appl. Opt.* 50.9 (2011), pp. C164–C171. doi: 10.1364/AO.50.00C164.
- [94] S. Schröder, D. Unglaub, M. Trost, X. Cheng, J. Zhang and A. Duپarre: *Spectral angle-resolved scattering of thin film coatings*. In: *Appl. Opt.* 53.4 (2014), A35–A41. doi: 10.1364/AO.53.000A35.
- [95] J. Schwinger: *On the Classical Radiation of Accelerated Electrons*. In: *Physical Review* 75.12 (1949), pp. 1912–1925. doi: 10.1103/PhysRev.75.1912.
- [96] J. Schermann: *The theoretical derivation of fluorescence X-ray intensities from mixtures*. In: *Spectrochimica Acta* 7 (1955), pp. 283–306. doi: 10.1016/0371-1951(55)80041-0.

- [97] T. Shiraishiwa and N. Fujino: Theoretical Calculation of Fluorescent X-Ray Intensities in Fluorescent X-Ray Spectrochemical Analysis, In: *Japanese Journal of Applied Physics* 5.10 (1966), p. 886. doi: 10.1143/JJAP.5.886.
- [98] P. Siffalovic, E. Majkova, L. Chitru, M. Jergel, S. Luby, J. Keckes, G. Mayer, A. Timman, S. V. Roth, T. Tsuru, T. Harada, M. Yamamoto and U. Heinemann: Characterization of Mo/Si soft X-ray multilayer mirrors by grazing-incidence small-angle X-ray scattering, In: *Vacuum* 84.1 (2009), pp. 19–25. doi: <http://dx.doi.org/10.1016/j.vacuum.2009.04.026>.
- [99] S. K. Sinha: X-ray diffuse scattering as a probe for thin film and interface structure, In: *J. Phys. III France* 4.9 (1994), pp. 1543–1557. doi: 10.1051/jphys:1994221.
- [100] S. K. Sinha, E. B. Sirrotta, S. Garoff and H. B. Stanley: X-ray and neutron scattering from rough surfaces, In: *Phys. Rev. B* 38.4 (1988), pp. 2297–2311. doi: 10.1103/PhysRevB.38.2297.
- [101] V. Soltwisch, A. Haase, J. Wernerke, J. Probst, M. Schonegen, S. Burger, M. Krumrey and F. Scholze: Correlated diffuse x-ray scattering from periodically nanostructured surfaces, In: *Physical Review B* 94.3 (2016), p. 035419. doi: 10.1103/PhysRevB.94.035419.
- [102] V. Soltwisch, A. Fischer, C. Laubis, C. Stadelhofer, F. Scholze and A. Ulrich: Polarization resolved measurements with the new EUV ellipsometer of PTB, In: *SPIE. Vol. 9422. 2015*, pp. 942213–7. doi: 10.1117/12.2085798.
- [103] E. Spiller: Low-Loss Reflection Coatings Using Absorbing Materials, In: *Applied Physics Letters* 20.9 (1972), pp. 365–367. doi: <http://dx.doi.org/10.1063/1.1654189>.
- [104] E. Spiller, D. Stearns and M. Krumrey: Multilayer X-ray mirrors: Interfacial roughness, scattering, and image quality, In: *Journal of applied physics* 74.1 (1993), pp. 107–118.
- [105] D. G. Stearns: X-ray scattering from interfacial roughness in multilayer structures, In: *Journal of Applied Physics* 71.9 (1992), pp. 4286–4298. doi: 10.1063/1.350810.
- [106] D. G. Stearns, R. S. Rosen and S. P. Vermon: Fabrication of high-refractance Mo-Si multilayer mirrors by planar-magnetron sputtering, In: *Journal of Vacuum Science & Technology A: Vacuum, Surfaces, and Films* 9.5 (1991), pp. 2662–2669. doi: 10.1116/1.577221.
- [107] A. C. Thompson and D. Vaughan, eds.: *X-ray Data Booklet*. Second, Lawrence Berkeley National Laboratory, University of California, 2001.
- [108] R. Thorngren, R. Klein and G. Ulm: The electron storage ring BESSY II as a primary source standard from the visible to the X-ray range, In: *Metrologia* 38.5 (2001), p. 385. doi: 10.1088/0026-1394/38/5/3.
- [109] M. Toyoda, Y. Shitanai, M. Yanagihara, T. Ejima, M. Yamamoto and M. Watanabe: Soft-X-Ray Imaging Microscope with a Multilayer-Coated Schwarzschild Objective: Imaging Tests, In: *Japanese Journal of Applied Physics* 39. Part 1, No. 4A (2000), pp. 1926–1929. doi: 10.1143/JJAP.39.1926.
- [110] J. Tummel, H. Blume, G. Brandt, J. Eden, B. Meyer, H. Scherr, F. Scholz, F. Scholze and G. Ulm: Characterization of the PTB EUV reflectometry facility for large EUVL optical components, In: *Proc. SPIE* 5037 (2003), pp. 265–273. doi: 10.1117/12.482668.

- [111] J. Verhoeven, L. Chongguang, E. J. Puij, M. J. van der Wiel and T. P. Huijsen; Ion beam modification of Mo₂Si multilayer systems for X-ray reflection; In: *Applied Surface Science* **55.2** (1992), pp. 97–103. doi: 10.1016/0169-4332(92)90099-1.
- [112] B. Vidal and P. Vincent; Metallic multilayers for x rays using classical thin-film theory; en. In: *Applied Optics* **23.11** (1984), p. 1794. doi: 10.1364/AO.23.001794.
- [113] S. N. Yakunin, I. A. Makhotkin, K. V. Nikolaev, R. W. E. v. d. Kruijs, M. A. Chuev and F. Bijkerk; Combined EUV reflectance and X-ray reflectivity data analysis of periodic multilayer structures; In: *Opt. Express* **22.17** (2014), pp. 20076–20086. doi: 10.1364/OE.22.020076.
- [114] S. A. Yulin, F. Schaefers, T. Feigl and N. Kaiser; High-performance Cr/Sc multilayers for the soft x-ray range; In: *Proc. SPIE* **5193** (2004), pp. 172–176. doi: 10.1117/12.505688.

